

# Weak and entropy physics-informed neural networks for conservation laws

Ismail Oubarka<sup>a,b,\*</sup>, Imad Kissami<sup>a</sup>, Mohamed Boubekour<sup>b</sup>, Fayssal Benkhaldoun<sup>b</sup>, Aziz Madrane<sup>c</sup>, Zakaria Saâdi<sup>d</sup>

<sup>a</sup>Mohammed VI Polytechnic University, College of Computing, Lot 660, Ben Guerir, 43150, Morocco

<sup>b</sup>LAGA, CNRS, UMR 7539, Université Sorbonne Paris Nord, Villetaneuse, 93430, France

<sup>c</sup>Department of Mechanical Engineering, McGill University, Montreal, QC H3A 2T8, Canada

<sup>d</sup>Autorité de Sûreté Nucléaire et de Radioprotection (ASNR), PSE-ENV/SPDR/UEMIS, F-92260, Fontenay-aux-Roses, France

---

## Abstract

We propose Weak and Entropy PINNs (WE-PINNs) for the approximation of entropy solutions to nonlinear hyperbolic conservation laws. Standard physics-informed neural networks enforce governing equations in strong differential form, an approach that becomes structurally inconsistent in the presence of discontinuities due to the divergence of strong-form residuals near shocks. The proposed method replaces pointwise residual minimization with a space–time weak formulation derived from the divergence theorem. Conservation is enforced through boundary flux integrals over dynamically sampled space–time control volumes, yielding a mesh-free control-volume framework that remains well-defined for discontinuous solutions. Entropy admissibility is incorporated in integral form to ensure uniqueness and physical consistency of the weak solution. The resulting loss functional combines space–time flux balance and entropy inequalities, without resorting to dual-norm saddle-point formulations, auxiliary potential networks, or fixed discretization meshes. This makes the proposed method remarkably easy to implement, requiring only a simple standard neural network architecture. We establish a rigorous convergence analysis linking the network’s loss function to the  $L^1$  error towards the entropy solution, providing the first explicit  $L^1$  convergence rate for a mesh-free control-volume PINN formulation via the Bouchut-Perthame framework for scalar conservation laws. Numerical experiments on the Burgers equation, the shallow water equations, and the compressible Euler equations demonstrate accurate shock resolution and robust performance in both smooth and shock-dominated regimes.

*Keywords:* PINNs, Hyperbolic conservation laws, Weak entropy formulation, space–time control volumes,  $L^1$  convergence, TVD regularization

---

## 1. Introduction

Nonlinear conservation laws arise in a wide range of scientific and engineering applications, including compressible fluid dynamics, shallow water flows, gas dynamics, and related transport phenomena [1, 2, 3, 4, 5]. These models describe the evolution of conserved physical quantities and play a central role in the mathematical formulation of wave propagation problems. A distinctive feature of nonlinear conservation laws is the spontaneous formation of discontinuities, commonly referred to as shock waves, even when the initial conditions are smooth [3, 6, 7, 8]. This behavior is an intrinsic property of the governing equations and not a consequence of numerical approximation. The emergence of shocks invalidates classical smooth solution concepts and requires the interpretation of solutions in a weak sense that admits discontinuities [3, 9]. An additional theoretical difficulty is that weak solutions are, in general, not unique. The selection of the physically relevant solution requires the enforcement of entropy conditions, which express the second law of thermodynamics or analogous admissibility principles [1, 3, 9]. Consequently, the numerical approximation of conservation laws must simultaneously ensure conservation in the weak sense and enforce appropriate entropy constraints to guarantee physical consistency.

---

\*Corresponding author

Email address: ismail.oubarka@um6p.com (Ismail Oubarka)

Physics-Informed Neural Networks (PINNs), introduced by Raissi et al. [10], have emerged as a promising framework for solving partial differential equations using deep learning. The central idea of PINNs is to embed the governing equations into the loss function of a neural network, allowing the model to learn solutions that satisfy both observational data and physical constraints. This approach has demonstrated strong performance for a variety of problems, particularly for smooth solutions of elliptic and parabolic equations, as well as certain time-dependent PDEs [11, 12, 13]. Despite their success in diffusion-dominated and smooth regimes, standard PINNs encounter significant difficulties when applied to hyperbolic conservation laws. In the classical formulation, the governing equations are enforced in strong differential form by minimizing a pointwise residual. While this strategy is effective for smooth solutions, it becomes problematic when discontinuities arise. Shock waves and other non-smooth structures invalidate classical derivatives, leading to instability, slow convergence, or excessive numerical diffusion in the learned solution. Several studies have reported that standard PINNs tend to oversmooth discontinuities and struggle to accurately capture sharp gradients in problems such as the Burgers equation, shallow water equations, and compressible Euler equations (see, e.g., [14, 15, 12, 16]). These challenges are closely related to the strong-form residual minimization, which implicitly favors smooth approximations and does not naturally enforce conservation in the weak sense. Moreover, the entropy condition, which is essential for selecting the physically admissible solution, is not inherently incorporated into the classical PINN framework. These limitations indicate that a reformulation of PINNs is necessary when addressing nonlinear conservation laws, particularly in regimes where discontinuities and entropy constraints play a fundamental role.

Recent studies have demonstrated that the failure of classical PINNs for nonlinear hyperbolic conservation laws is not merely a practical issue related to network size or optimization, but rather a structural limitation of strong-form residual minimization. In particular, it has been shown that when a neural approximation sharpens toward a discontinuous entropy solution, the  $L^2$  norm of the strong-form residual may diverge, creating an optimization barrier that repels the training process away from the physically correct shock profile [17, 18]. This theoretical insight explains why classical PINNs tend to converge to overly smooth approximations even when sufficient model capacity is available.

Several strategies have been proposed to mitigate this difficulty. A first line of work retains the strong-form residual while introducing stabilization mechanisms, such as adaptive residual sampling [14], gradient reweighting [19], artificial viscosity regularization, and enforcement of Rankine–Hugoniot conditions. Although these approaches improve empirical robustness, the governing equations remain enforced pointwise in differential form, and shock resolution typically depends sensitively on hyperparameter choices.

A second direction incorporates ideas from finite-volume discretizations. Control-volume PINNs [20] enforce conservation through space–time flux balances over discrete control volumes, while architectures such as SFVnet [21] embed finite-volume residuals into deep convolutional models for compressible flows. These methods significantly improve shock-capturing capability by mimicking classical numerical schemes. However, they are generally tied to predefined mesh structures and inherit a least-squares control-volume formulation, positioning them as hybrid neural-numerical solvers rather than fully continuous weak formulations.

More recently, weak PINNs (wPINNs) [17] have replaced the strong  $L^2$  residual with weak (dual) norms of the PDE residual, motivated by functional analytic arguments showing that discontinuous entropy solutions remain bounded in  $W^{-1,p}$ -type norms even when strong norms diverge. These approaches approximate dual norms through saddle-point optimization with auxiliary neural networks representing test functions, or by solving associated elliptic problems via neural networks. While mathematically rigorous, such formulations introduce additional adversarial networks and min–max optimization structures, increasing algorithmic complexity. This framework was subsequently extended by Chaumet and Giesselmann [22] to improve dual norm computation, handle boundary conditions more robustly, and generalize to systems of conservation laws.

Along similar lines, WF-PINNs [23] incorporate a weak-form integral loss based on test functions together with an entropy condition for the scalar Burgers equation. However, their formulation relies on smooth compactly supported test functions rather than boundary flux integrals, and the entropy condition is enforced pointwise rather than in integral form.

Another related development is the Coupled Integral PINN (CI-PINN) framework [18], which introduces auxiliary potential networks to enforce conservation in integral form. By coupling the state variable to its learned integral representation, these methods avoid direct differentiation of discontinuous primitives and improve robustness near shocks. Nevertheless, the resulting architecture requires dual-network coupling constraints and additional consistency

losses.

In contrast to these existing approaches, the proposed Weak and Entropy PINNs (WE-PINNs) adopt a direct space–time flux formulation derived from the divergence theorem. Conservation is enforced through boundary flux integrals over dynamically sampled space–time subdomains, without reliance on fixed meshes, discrete flux reconstruction, dual-norm estimation, or auxiliary potential networks. Entropy admissibility is incorporated in integral boundary form, and multi-scale space–time sampling is employed to ensure that moving discontinuities are consistently interrogated during training. This formulation provides a fully weak, geometrically interpretable framework for nonlinear conservation laws that remains mesh-free while preserving the physical structure of entropy solutions. More precisely, the proposed framework is designed to produce a loss function that:

- remains mathematically meaningful when the solution develops shocks, i.e. when classical derivatives  $u_t$  and  $\nabla u$  do not exist pointwise;
- enforces conservation in the sense of distributions, thereby incorporating the Rankine–Hugoniot jump conditions implicitly, with no special shock tracking required;
- selects the physically relevant entropy solution among the many weak solutions that may exist for nonlinear conservation laws;
- avoids the classical strong-form PINN residual  $\|u_t + \nabla \cdot F(u)\|^2$ , which typically biases the network towards over-smoothing shocks.

The central idea is to replace the strong-form PDE residual by space–time integral constraints on the boundary  $\partial D$  of many subdomains  $D \subset \Omega_{x,t}$ :

$$\int_{\partial D} (U n_t + F(U) \cdot n_x) dS = 0 \quad \text{for many (ideally all) } D.$$

Entropy inequalities in integral form are then added to recover uniqueness and physical admissibility.

The main contributions of this work are threefold: (i) a novel weak formulation that remains well-defined for discontinuous solutions, which is straightforward to implement and requires only a simple neural network architecture; (ii) a rigorous convergence analysis establishing that the  $L^1$  error is controlled by the explicit dual norm loss representation, providing a strong theoretical foundation for weak control-volume PINN formulations in the scalar case; (iii) comprehensive numerical validation on scalar equations and systems.

The paper is organized as follows. The mathematical background and weak formulation are presented in Section 2. The WE-PINNs framework, including the loss function, sampling strategy, and quadrature rules, is developed in Section 3. A convergence analysis framework linking the continuous weak error to the discrete loss function and establishing the  $L^1$  bound towards the entropy solution is presented in Section 4. Numerical experiments on the Burgers equation, the compressible Euler equations, and the shallow water equations are reported in Section 5. Finally, Section 6 concludes the paper.

## 2. Mathematical background and weak formulation

We consider a system of nonlinear conservation laws in divergence form

$$\partial_t U + \nabla_x \cdot F(U) = 0, \quad U : \Omega_{x,t} \rightarrow \mathbb{R}^m, \quad (1)$$

where  $\Omega_{x,t} = \Omega_x \times (0, T)$ ,  $U$  denotes the vector of conserved variables, and  $F : \mathbb{R}^m \rightarrow \mathbb{R}^{m \times d}$  is the flux function, assumed continuously differentiable. Writing the flux componentwise,

$$F(U) = (F^{(1)}(U), \dots, F^{(d)}(U)), \quad F^{(j)}(U) \in \mathbb{R}^m,$$

where  $F^{(j)}(U)$  represents the flux in the spatial direction  $x_j$ . Equation (1) expresses the local balance of the conserved quantities: the time variation of  $U$  inside any region equals the net flux entering or leaving that region. For the space–time formulation introduced below, it is convenient to work in  $(d + 1)$  dimensions. Given a space–time subdomain  $D \subset \Omega_{x,t}$ , the outward unit normal on  $\partial D$  is written  $n = (n_x, n_t) \in \mathbb{R}^{d+1}$ , with  $n_x \in \mathbb{R}^d$  and  $n_t \in \mathbb{R}$ , and  $dS$  denotes the surface measure on  $\partial D$ .

### 2.1. Weak conservation in space–time

Since solutions of nonlinear conservation laws may develop shock discontinuities in finite time, classical derivatives  $\partial_t U$  and  $\nabla_x U$  may cease to exist pointwise, and the differential form of equation (1) is no longer meaningful in the classical sense. Conservation must therefore be enforced in a weak sense. The conservation law holds in the weak sense if, for any smooth compactly supported test function  $\varphi \in C_c^1(\Omega_{x,t}; \mathbb{R}^m)$ , the following integral identity holds:

$$\int_0^T \int_{\Omega_x} \left( U \cdot \partial_t \varphi + \sum_{j=1}^d F^{(j)}(U) \cdot \partial_{x_j} \varphi \right) dx dt = 0.$$

This identity remains well-defined even when  $U$  contains discontinuities, provided  $U$  and  $F(U)$  are integrable, and allows shock solutions to be included naturally within the mathematical framework.

An equivalent and particularly convenient representation is obtained by rewriting (1) as a divergence in space–time. Defining the space–time flux

$$J(U) := (F(U), U) \in \mathbb{R}^{m \times (d+1)},$$

the conservation law reads  $\nabla_{x,t} \cdot J(U) = 0$ . Applying the divergence theorem over any subdomain  $D \subset \Omega_{x,t}$  yields the boundary conservation statement

$$\int_{\partial D} (U n_t + F(U) \cdot n_x) dS = 0, \quad \forall D \subset \Omega_{x,t}. \quad (2)$$

This identity expresses that the total variation of the conserved quantities inside  $D$  is balanced by the net flux across its boundary. The equality is vector-valued, with one equation satisfied for each conserved component. Crucially, this formulation remains valid in the presence of shocks: the Rankine–Hugoniot jump conditions are implicitly contained in (2), so no explicit shock tracking is required to enforce conservation across discontinuities.

### 2.2. Entropy condition and admissibility

Although the weak formulation (2) accommodates discontinuous solutions, it does not guarantee uniqueness. Nonphysical weak solutions, such as expansion shocks, may satisfy the conservation law in the distributional sense. An additional selection criterion is therefore required. This selection mechanism is provided by the entropy condition.

An entropy pair consists of a convex entropy function  $\eta : \mathbb{R}^m \rightarrow \mathbb{R}$  together with associated entropy fluxes

$$q(U) = (q^{(1)}(U), \dots, q^{(d)}(U)), \quad q^{(j)} : \mathbb{R}^m \rightarrow \mathbb{R},$$

satisfying the compatibility relations

$$\nabla_U q^{(j)}(U) = \nabla_U \eta(U) \nabla_U F^{(j)}(U), \quad j = 1, \dots, d.$$

When  $U$  is smooth, the entropy satisfies the additional conservation law  $\partial_t \eta(U) + \nabla_x \cdot q(U) = 0$ . However, when discontinuities are present, entropy may be produced across shocks. The physically admissible solution must therefore satisfy the entropy *inequality*

$$\partial_t \eta(U) + \nabla_x \cdot q(U) \leq 0$$

in the distributional sense. This condition rules out nonphysical weak solutions and ensures uniqueness in many important cases, including scalar conservation laws and several physically relevant systems. As in the case of weak conservation, integrating over an arbitrary space–time subdomain  $D$  and applying the divergence theorem yields the integral form

$$\int_{\partial D} (\eta(U) n_t + q(U) \cdot n_x) dS \leq 0, \quad \forall D \subset \Omega_{x,t}. \quad (3)$$

While weak conservation provides an equality that enforces balance of the conserved quantities, the entropy condition introduces a one-sided constraint that selects the physically admissible solution. Together, (2) and (3) characterize the entropy solution of (1), and both identities serve as the direct basis for the loss function constructed in Section 3.

### 3. Weak and Entropy PINN formulation (WE-PINNs)

The WE-PINNs framework is built on a direct space–time integral formulation of conservation and entropy admissibility. Rather than enforcing the governing equations pointwise in differential form, the method penalizes violations of the weak conservation identity and the entropy inequality over a collection of dynamically sampled space–time control volumes. This section presents the construction of the loss function, the sampling strategy, and the quadrature rules used to evaluate the boundary integrals.

#### 3.1. Space–time control-volume formulation

The space–time conservation identity (2) serves as the structural foundation of the WE-PINNs framework. Rather than enforcing conservation pointwise in differential form, the method enforces this identity over space–time control volumes, thereby avoiding the need for classical differentiability. We restrict attention to control volumes of the form

$$D = K \times [t^-, t^+] \subset \Omega_{x,t},$$

where  $K \subset \Omega_x$  is a bounded spatial region with sufficiently regular boundary  $\partial K$ . No restriction is imposed on the geometry of  $K$  beyond the regularity required for the divergence theorem to apply. Decomposing the boundary  $\partial D$  into the two time faces  $K \times \{t^-\}$ ,  $K \times \{t^+\}$ , and the lateral boundary  $\partial K \times [t^-, t^+]$ , the space–time conservation identity reduces to the balance relation

$$\int_K U(x, t^+) dx - \int_K U(x, t^-) dx + \int_{t^-}^{t^+} \int_{\partial K} F(U) \cdot n_x dS_x dt = 0.$$

This relation expresses conservation over the spatial region  $K$ : the change of the conserved quantities inside  $K$  between times  $t^-$  and  $t^+$  is exactly balanced by the net flux across its spatial boundary. The formulation is independent of the spatial dimension  $d$  (see Appendix A for more details) and remains valid even in the presence of shock discontinuities, since it follows directly from the space–time divergence theorem without requiring pointwise differentiability of  $U$ . This control-volume identity forms the basis of the weak conservation loss introduced in Section 3.2. The spatial distribution of collocation points and their associated space–time control volumes is illustrated in Figure 1.

**Axis-aligned control volumes.** For stability and simplicity, we use axis-aligned rectangles in 1D and boxes in higher dimensions:

$$D = [x_1, x_2] \times [t_1, t_2] \quad (d = 1),$$

and similarly in  $d = 2$  and  $d = 3$  with Cartesian products of spatial intervals. With this choice, the outward normal vector  $n = (n_x, n_t)$  is constant on each face of  $\partial D$ , which considerably simplifies the evaluation of the boundary integrals appearing in the weak and entropy residuals.

**Multi-scale sampling.** Shocks are localized structures, and enforcing conservation at a single spatial or temporal scale is not sufficient. We therefore sample control volumes with variable sizes

$$\ell_x = x_2 - x_1 \in [\ell_{\min}, \ell_{\max}], \quad \ell_t = t_2 - t_1 \in [\tau_{\min}, \tau_{\max}].$$

Large domains promote global balance of conserved quantities, while smaller domains increase sensitivity to sharp gradients. Mixing multiple scales improves robustness and prevents the training process from ignoring localized shock structures.

**One spatial dimension.** Each boundary face reduces to a one-dimensional integral. We use Gauss–Legendre quadrature, which provides high accuracy with relatively few evaluation points:

$$\int_a^b g(s) ds \approx \frac{b-a}{2} \sum_{q=1}^Q w_q g\left(\frac{a+b}{2} + \frac{b-a}{2} \xi_q\right),$$

where  $\{\xi_q, w_q\}_{q=1}^Q$  are the standard Gauss nodes and weights on  $[-1, 1]$ . Deterministic quadrature rules are preferred over Monte Carlo estimates, as they yield smooth loss functions that are considerably easier to optimize, particularly in the early stages of training.

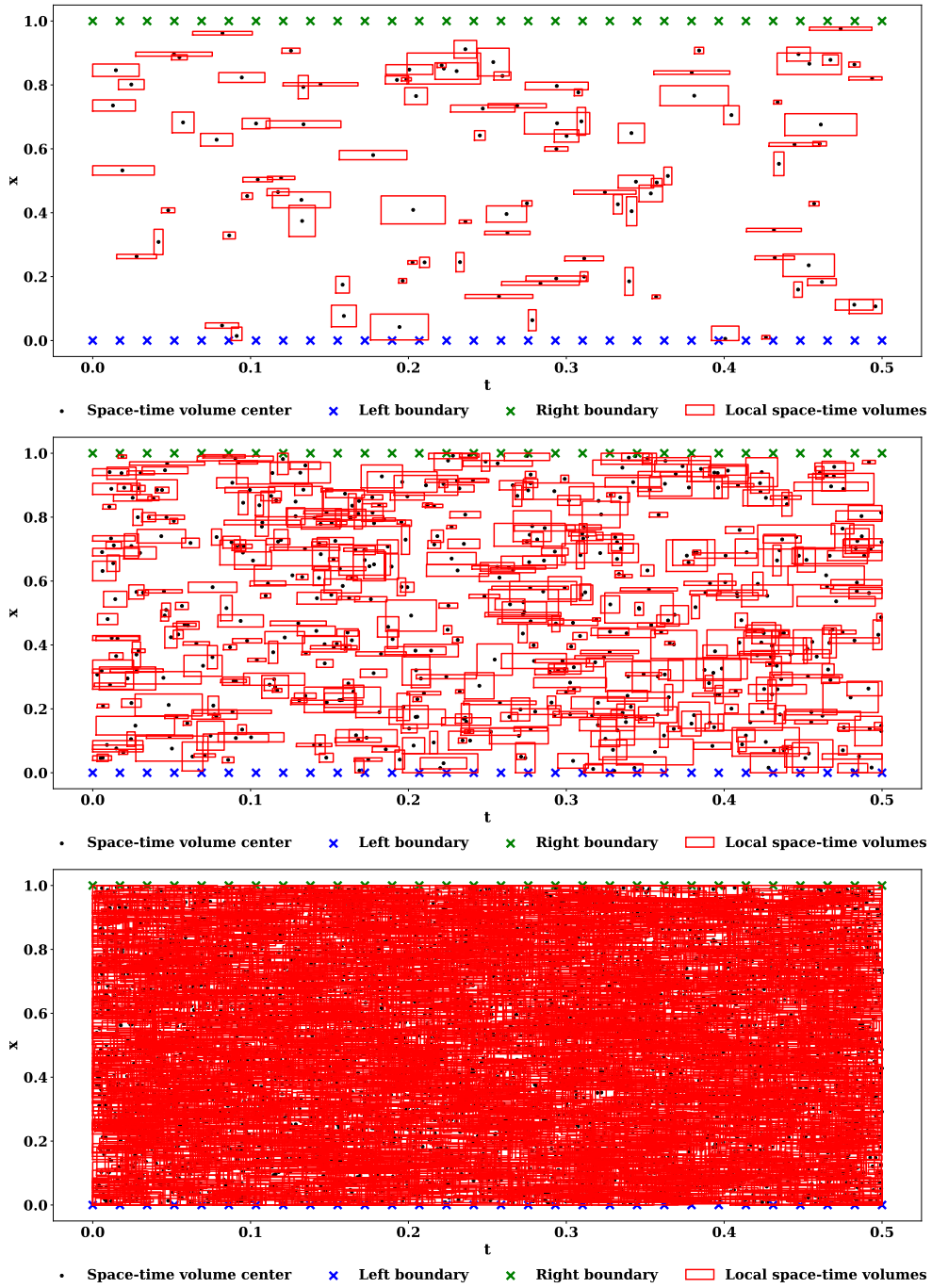


Figure 1: Local space–time control volumes. Each collocation point defines the center of a control volume  $D_k$  over which the conservation identity (2) is enforced. The illustrations show different sampling densities of the space–time control volumes: 100 (top), 500 (middle), and 5000 (bottom).

**Two and three spatial dimensions.** In higher dimensions, each boundary face is rectangular and we apply tensor-

product Gauss–Legendre rules. In two spatial dimensions,

$$\int_{x_1}^{x_2} \int_{y_1}^{y_2} g(x, y) dx dy \approx \frac{(x_2 - x_1)(y_2 - y_1)}{4} \sum_{p=1}^{Q_x} \sum_{q=1}^{Q_y} w_p v_q g(x(\xi_p), y(\eta_q)),$$

where the mapping from  $[-1, 1]^2$  to the physical face is performed independently in each coordinate direction. The same tensor-product strategy extends straightforwardly to three spatial dimensions. The combination of multi-scale adaptive sampling and accurate deterministic quadrature ensures that the weak and entropy residuals are evaluated reliably throughout the entire space–time domain, including in regions containing shocks.

### 3.2. Weak conservation loss

Let  $U_\theta(x, t)$  denote the neural network approximation of the conserved variables, parameterized by  $\theta$ . To satisfy the initial condition exactly, we employ a temporal ansatz:

$$U_\theta(x, t) = (1 - \tau(t))U_0(x) + \tau(t)\mathcal{N}_\theta(x, t),$$

where  $\tau(t)$  is a differentiable function with  $\tau(0) = 0$  and  $\tau(T) = 1$  (e.g.,  $\tau(t) = t/T$ ), and  $\mathcal{N}_\theta$  is a standard neural network. This construction guarantees  $U_\theta(x, 0) \equiv U_0(x)$ , eliminating the initial condition error term from the convergence analysis. The weak space–time control-volume formulation is enforced numerically by penalizing violations of the conservation identity over the collection  $\{D_k\}_{k=1}^{N_D}$ . For each control volume  $D_k \subset \Omega_{x,t}$ , the weak conservation residual is defined as

$$R_\theta(D_k) = \int_{\partial D_k} (U_\theta n_t + F(U_\theta) \cdot n_x) dS.$$

This residual measures the imbalance of fluxes across the boundary of  $D_k$  and therefore quantifies the deviation of the neural approximation from exact conservation over that volume. Since conservation holds componentwise, the residual is vector-valued,  $R_\theta(D_k) \in \mathbb{R}^m$ , with one component corresponding to each conserved quantity. Crucially, boundary conditions are seamlessly integrated into this formulation. When a boundary face of a control volume  $D_k$  coincides with the physical boundary of the domain  $\Omega_x$ , the flux integration across this face directly enforces the prescribed boundary conditions naturally through the evaluation of  $R_\theta(D_k)$ . The weak conservation loss is defined as the volume-weighted average of the squared Euclidean norm of these residuals:

$$L_{\text{cons}}(\theta) = \frac{1}{N_D} \sum_{k=1}^{N_D} \frac{\|R_\theta(D_k)\|_2^2}{|D_k|}.$$

This formulation enforces conservation in an integral rather than pointwise sense, thereby remaining consistent with discontinuous solutions. Because the loss depends exclusively on boundary flux integrals, it avoids the explicit evaluation of spatial derivatives of  $U_\theta$ , which enhances stability in regimes characterized by steep gradients or shock discontinuities. The enforcement of the conservation constraint over multiple space–time control volumes distributed throughout the domain ensures that the balance law is respected locally while preserving global consistency.

### 3.3. Entropy inequality loss

To enforce physical admissibility and select the entropy-consistent solution, an additional constraint based on the entropy inequality (3) is incorporated into the loss functional. For each space–time control volume  $D_k$ , the entropy residual is defined as

$$E_\theta(D_k) = \int_{\partial D_k} (\eta(U_\theta) n_t + q(U_\theta) \cdot n_x) dS.$$

For entropy solutions, the space–time formulation requires that  $E_\theta(D_k) \leq 0$  for all admissible control volumes. Accordingly, only violations of this inequality are penalized, through a one-sided volume-weighted quadratic loss:

$$L_{\text{ent}}(\theta) = \frac{1}{N_D} \sum_{k=1}^{N_D} \frac{(\max\{0, E_\theta(D_k)\})^2}{|D_k|}.$$

This construction enforces entropy admissibility in a manner consistent with the underlying theory: the inequality is preserved whenever it is satisfied, while positive deviations corresponding to entropy violations are penalized. Crucially, equality is not enforced, since entropy production across shocks is physically admissible. The entropy loss therefore complements the weak conservation loss by introducing a one-sided constraint that selects the physically relevant weak solution without suppressing shock dissipation.

### 3.4. Total Variation Diminishing (TVD) regularization

The Bouchut-Perthame estimate [24], which forms the foundation of our convergence analysis, requires a uniform bound on the total variation:

$$\sup_{t \in [0, T]} TV(U_\theta(\cdot, t)) < \infty,$$

where the total variation is defined as

$$TV(U_\theta(\cdot, t)) = \int_{\Omega} |\nabla_x U_\theta(x, t)| dx.$$

To guarantee this condition, we introduce a TVD regularization term:

$$L_{\text{TVD}}(\theta) = \sup_{t \in [0, T]} \int_{\Omega} |\nabla_x U_\theta(x, t)| dx.$$

In practice, at each training iteration, the supremum and the spatial integrals are evaluated by sampling a random cloud of points distributed across the space–time domain, allowing for efficient stochastic approximation of the total variation:

$$L_{\text{TVD}}(\theta) \approx \max_{j=1, \dots, N_t} \sum_{k=1}^{N_x-1} |U_\theta(x_{k+1}, t_j) - U_\theta(x_k, t_j)|,$$

where the coordinates  $(x_k, t_j)$  are drawn randomly at each step.

### 3.5. Total loss function

The complete WE-PINNs objective is defined as

$$L(\theta) = \lambda_1 L_{\text{cons}} + \lambda_2 L_{\text{ent}} + \lambda_{\text{TVD}} L_{\text{TVD}},$$

where the weighting parameters are simply set to  $\lambda_1 = 1$ ,  $\lambda_2 = 1$ , and  $\lambda_{\text{TVD}} = 1$ . Minimizing  $L(\theta)$  simultaneously enforces the space–time flux balance, the entropy inequality, and bounded variation over the sampled regions of the domain.

## 4. Convergence Analysis

In this section, we establish the theoretical foundations for the convergence of WE-PINNs. The analysis relies on three key components: quantifying the continuous weak truncation error via dual norms, linking this error to the discrete network losses over control volumes, and applying the Bouchut-Perthame error estimates. We emphasize that this convergence result is currently valid only for scalar conservation laws.

### 4.1. Weak Entropy Truncation Error

Let  $\{D_i\}_{i=1}^{N_D}$  be a partition of the space–time domain  $\Omega \times (0, T)$  into control volumes. To evaluate how well the neural approximation  $U_\theta$  satisfies the conservation law and the entropy condition in the sense of distributions, we define the continuous weak truncation error  $E_R(U_\theta)$ . Following Bouchut and Perthame [24], this error is defined as the supremum of the entropy residual over a specific class of test functions:

$$E_R(U_\theta) = \sup_{k \in \mathbb{R}, \varphi \in \mathcal{A}} \mathcal{R}_{k, \varphi}(U_\theta),$$

where the residual functional is given by

$$\mathcal{R}_{k,\varphi}(U_\theta) = \int_0^T \int_\Omega (|U_\theta - k| \partial_t \varphi + \text{sgn}(U_\theta - k)(F(U_\theta) - F(k)) \cdot \nabla_x \varphi) dx dt.$$

Crucially, the supremum is taken over the test function space  $\mathcal{A}$ :

$$\mathcal{A} = \{\varphi \in C_c^\infty(\Omega \times (0, T)) : \varphi \geq 0, \|\partial_t \varphi\|_{L^\infty} + \|\nabla_x \varphi\|_{L^\infty} \leq 1\}.$$

The constraint on the Lipschitz constant of  $\varphi$  (bounded by 1) translates the error into a dual norm (analogous to the  $W^{-1,1}$  norm). This is strictly necessary to yield a finite, measurable error quantity that does not blow up across shock discontinuities.

**Lemma 1** (Link Between Discrete Losses and Weak Truncation Error). *For any partition  $\{D_i\}_{i=1}^{N_D}$  of  $\Omega \times (0, T)$ , the continuous weak truncation error is bounded by the volume-weighted network losses:*

$$E_R(U_\theta) \leq \sqrt{|\Omega \times (0, T)|} \cdot (\sqrt{L_{\text{cons}}(\theta)} + \sqrt{L_{\text{ent}}(\theta)}).$$

*Proof.* For a fixed  $k \in \mathbb{R}$  and  $\varphi \in \mathcal{A}$ , we decompose the integral  $\mathcal{R}_{k,\varphi}(U_\theta)$  over the control volumes  $D_i$ . Applying the divergence theorem on each  $D_i$ , the continuous residual translates into boundary flux integrals, corresponding exactly to the local conservation residual  $R_{\text{cons}}(D_i)$  and entropy residual  $R_{\text{ent}}(D_i, k)$ . Applying the triangle inequality and Hölder's inequality, we bound the integral by factoring out the derivatives of  $\varphi$ :

$$\mathcal{R}_{k,\varphi}(U_\theta) \leq \sum_{i=1}^{N_D} (\|\partial_t \varphi\|_{L^\infty} + \|\nabla_x \varphi\|_{L^\infty}) \cdot (|R_{\text{cons}}(D_i)| + |R_{\text{ent}}(D_i, k)|).$$

Since  $\varphi \in \mathcal{A}$ , its Lipschitz constant is bounded by 1. The factor containing  $\varphi$  is therefore neutralized:

$$\mathcal{R}_{k,\varphi}(U_\theta) \leq 1 \cdot \sum_{i=1}^{N_D} (|R_{\text{cons}}(D_i)| + |R_{\text{ent}}(D_i, k)|).$$

To connect this to the WE-PINNs volume-weighted loss functions, we multiply and divide by  $\sqrt{|D_i|}$  and apply the discrete Cauchy-Schwarz inequality:

$$\sum_{i=1}^{N_D} |R_{\text{cons}}(D_i)| = \sum_{i=1}^{N_D} \frac{|R_{\text{cons}}(D_i)|}{\sqrt{|D_i|}} \sqrt{|D_i|} \leq \left( \sum_{i=1}^{N_D} \frac{|R_{\text{cons}}(D_i)|^2}{|D_i|} \right)^{1/2} \left( \sum_{i=1}^{N_D} |D_i| \right)^{1/2}.$$

Recognizing that  $\sum |D_i| = |\Omega \times (0, T)|$  and substituting the definitions of  $L_{\text{cons}}(\theta)$  and  $L_{\text{ent}}(\theta)$  defined in Section 3, we obtain the upper bound for any  $\varphi \in \mathcal{A}$ . Taking the supremum over  $k$  and  $\varphi$  concludes the proof.  $\square$

#### 4.2. Bouchut-Perthame Error Estimate

The following fundamental result provides an  $L^1$  error estimate for approximate solutions of scalar conservation laws.

**Theorem 1** (Bouchut-Perthame [24]). *Let  $u$  be the unique entropy solution of (1) with initial condition  $u_0 \in L^\infty(\Omega) \cap BV(\Omega)$ . Let  $v$  be an approximate solution satisfying:*

- $v$  is bounded and measurable;
- $\sup_{t \in [0, T]} TV(v(\cdot, t)) < \infty$ .

Then, for any  $T > 0$ ,

$$\|v(\cdot, T) - u(\cdot, T)\|_{L^1(\Omega)} \leq \|v(\cdot, 0) - u_0\|_{L^1(\Omega)} + C \sqrt{TV(u_0) \cdot \sup_{t \in [0, T]} TV(v(\cdot, t))} \cdot \sqrt{E_R(v)},$$

where  $C$  is a constant depending only on the Lipschitz constant of the flux  $F$ .

### 4.3. Main Convergence Theorem

**Theorem 2** (Convergence of WE-PINNs). *Let  $u$  be the entropy solution of (1) with initial condition  $u_0 \in L^\infty(\Omega) \cap BV(\Omega)$ . Let  $U_\theta$  be the neural network approximation defined by the temporal ansatz with parameters  $\theta$ . Assume that:*

1. *The flux  $F$  is Lipschitz continuous;*
2. *The TVD regularization guarantees  $\sup_{t \in [0, T]} TV(U_\theta(\cdot, t)) \leq M$  for some constant  $M$ ;*
3. *The weak conservation loss satisfies  $L_{\text{cons}}(\theta) \rightarrow 0$ ;*
4. *The entropy loss satisfies  $L_{\text{ent}}(\theta) \rightarrow 0$ .*

*Then, there exists a constant  $K_{\text{opt}}$  independent of  $\theta$  such that*

$$\|U_\theta(\cdot, T) - u(\cdot, T)\|_{L^1(\Omega)} \leq K_{\text{opt}} \cdot (L_{\text{cons}}(\theta)^{1/4} + L_{\text{ent}}(\theta)^{1/4}).$$

*Consequently, as  $L_{\text{cons}}(\theta) \rightarrow 0$  and  $L_{\text{ent}}(\theta) \rightarrow 0$  simultaneously,  $U_\theta$  converges to the unique physically admissible entropy solution  $u$  in  $L^1(\Omega)$ .*

*Proof.* We apply the Bouchut-Perthame estimate with  $v = U_\theta$ .

**Step 1: Initial condition error.** By construction of the temporal ansatz,  $U_\theta(x, 0) = u_0(x)$  for all  $x \in \Omega$ . Therefore,

$$\|U_\theta(\cdot, 0) - u_0\|_{L^1(\Omega)} = 0.$$

**Step 2: Total variation bound.** The TVD regularization term ensures the existence of a constant  $M$  such that

$$\sup_{t \in [0, T]} TV(U_\theta(\cdot, t)) \leq M.$$

**Step 3: Weak truncation error bound.** From Lemma 1, the continuous entropy defect is bounded by the network losses:

$$E_R(U_\theta) \leq \sqrt{|\Omega \times (0, T)|} \cdot (\sqrt{L_{\text{cons}}(\theta)} + \sqrt{L_{\text{ent}}(\theta)}).$$

The explicit inclusion of  $L_{\text{ent}}(\theta)$  is strictly necessary here to ensure that the neural network approximation does not violate the unilateral entropy constraints, preventing convergence to non-physical solutions such as expansion shocks.

**Step 4: Substitution.** Inserting into the Bouchut-Perthame estimate:

$$\begin{aligned} \|U_\theta(\cdot, T) - u(\cdot, T)\|_{L^1(\Omega)} &\leq C \sqrt{TV(u_0)} \cdot M \cdot \sqrt{E_R(U_\theta)} \\ &\leq C \sqrt{TV(u_0)} M \cdot [|\Omega \times (0, T)|^{1/2} (\sqrt{L_{\text{cons}}(\theta)} + \sqrt{L_{\text{ent}}(\theta)})]^{1/2}. \end{aligned}$$

Using the subadditive inequality  $(a + b)^{1/2} \leq a^{1/2} + b^{1/2}$  and defining  $K_{\text{opt}} = C \sqrt{TV(u_0)} M \cdot |\Omega \times (0, T)|^{1/4}$ , we obtain:

$$\|U_\theta(\cdot, T) - u(\cdot, T)\|_{L^1(\Omega)} \leq K_{\text{opt}} \cdot (L_{\text{cons}}(\theta)^{1/4} + L_{\text{ent}}(\theta)^{1/4}).$$

This rigorously controls the  $L^1$  error via the joint minimization of the weak flux balance and the entropy production.  $\square$

**Remark 1.** *The convergence rate of 1/4 is optimal for arbitrary control volume partitions. For regular, structured grids, the rate can be improved to 1/2 [24]. The result is rigorously established for scalar conservation laws; extension to systems remains an active research area.*

### 4.4. Training procedure

The complete training procedure is summarized in Algorithm 1. The parameters are first optimized using Adam and then refined using L-BFGS algorithm [25, 26, 27]. The loss weights  $\lambda_1$ ,  $\lambda_2$ , and  $\lambda_{\text{TVD}}$  are all set to 1.

---

**Algorithm 1** Training algorithm for WE-PINNs

---

- 1: **Input:** initial condition  $U_0$ , flux  $F(U)$ , entropy pair  $(\eta, q)$ , domain  $\Omega_{x,t}$ , loss weights  $\lambda_1 = 1, \lambda_2 = 1, \lambda_{\text{TVD}} = 1$
  - 2: Initialize neural network parameters  $\theta$
  - 3: Construct temporal ansatz:  $U_\theta(x, t) = (1 - \tau(t))U_0(x) + \tau(t)\mathcal{N}_\theta(x, t)$
  - 4: **while** not converged **do**
  - 5:     Sample space–time subdomains  $\{D_k\}_{k=1}^{N_D}$  at multiple scales.
  - 6:     **for**  $k = 1$  to  $N_D$  **do**
  - 7:         Evaluate  $R_\theta(D_k)$  and  $E_\theta(D_k)$  via Gauss–Legendre quadrature on each face of  $\partial D_k$
  - 8:     **end for**
  - 9:     Compute  $L_{\text{cons}}$  and  $L_{\text{ent}}$  as in Sections 3.2–3.3
  - 10:     Sample a random cloud of points and compute  $L_{\text{TVD}}$  as in Section 3.4
  - 11:     Assemble  $L(\theta) = L_{\text{cons}} + L_{\text{ent}} + L_{\text{TVD}}$
  - 12:     Update  $\theta$  using the Adam optimizer:  $\theta \leftarrow \text{Adam}(\theta, \nabla_\theta L(\theta))$
  - 13:     Refine  $\theta$  using L-BFGS optimizer
  - 14: **end while**
  - 15: **Output:** Trained network  $U_\theta$
- 

## 5. Numerical Experiments

In this section, we present a series of numerical experiments designed to evaluate the accuracy, stability, and robustness of the proposed WE-PINNs. We begin with scalar nonlinear conservation laws to validate the method in controlled settings. After demonstrating its effectiveness on prototype problems, we consider increasingly challenging nonlinear equations. Finally, we assess the performance of the method on systems of hyperbolic conservation laws, including Euler equations and shallow water equations. The entropy pair associated with each model is provided in Appendix C.

### 5.1. Inviscid Burgers Equation

We evaluate the proposed WE-PINNs framework on the one-dimensional inviscid Burgers equation

$$\partial_t u + \partial_x \left( \frac{u^2}{2} \right) = 0, \quad (x, t) \in \Omega \times (0, T],$$

which serves as a canonical nonlinear conservation law exhibiting both smooth nonlinear transport and shock formation. All experiments are performed on the domain  $\Omega = [-1, 1]$  with final time  $T = 1$ . The neural network approximating the conserved variable  $u_\theta$  consists of 8 hidden layers with 80 neurons per layer and tanh activation functions. space–time control volumes are sampled dynamically across multiple spatial and temporal scales, see 1. Boundary flux integrals are evaluated using Gauss–Legendre quadrature on each control-volume face with 6 points. Conservation and entropy admissibility are enforced through the weak space–time flux formulation described in Section 2. The training is performed in two stages. The parameters are first optimized using the Adam algorithm to ensure stable initial descent, followed by Limited-memory Broyden–Fletcher–Goldfarb–Shanno (L-BFGS) optimization to refine convergence of the weak flux balance and entropy constraints. To quantify accuracy, we compute relative space–time errors

$$E_{L^p} = \frac{\|u_\theta - u\|_{L^p(\Omega_T)}}{\|u\|_{L^p(\Omega_T)}}, \quad p = 1, 2,$$

where  $\Omega_T = \Omega \times (0, T)$  and  $u$  denotes the exact entropy solution.

#### 5.1.1. Riemann Shock Problem

We first consider the discontinuous initial condition

$$u(x, 0) = \begin{cases} 1, & x \leq -0.25, \\ 0, & x > -0.25, \end{cases}$$

for which the entropy solution consists of a single shock propagating with Rankine–Hugoniot speed  $s = \frac{1}{2}$ . This configuration directly tests the ability of WE-PINNs to resolve a moving discontinuity without artificial diffusion. Figure 2 shows the numerical solution at selected times. The shock propagates at the correct speed and remains sharply localized. No spurious oscillations or overshoots are observed near the discontinuity, and the constant states on either side are preserved. The corresponding relative errors are summarized in Table 1.

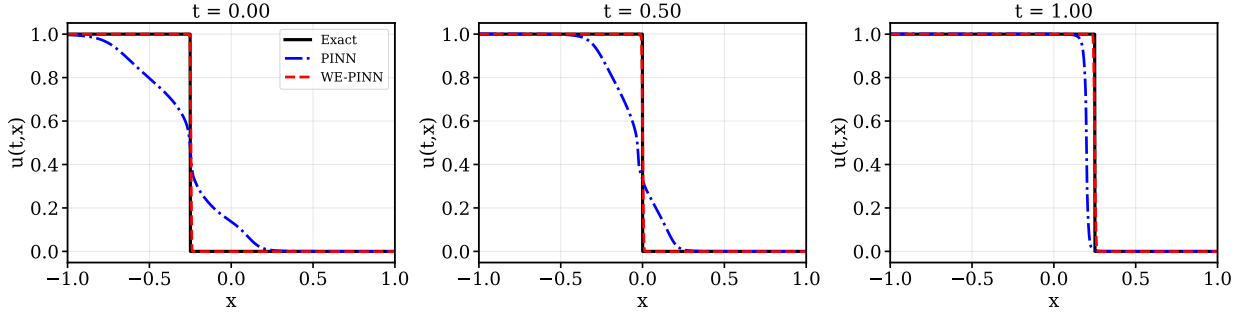


Figure 2: WE-PINNs solution of Riemann problem for the inviscid Burgers equation. The numerical solution is shown at selected times together with the exact entropy solution.

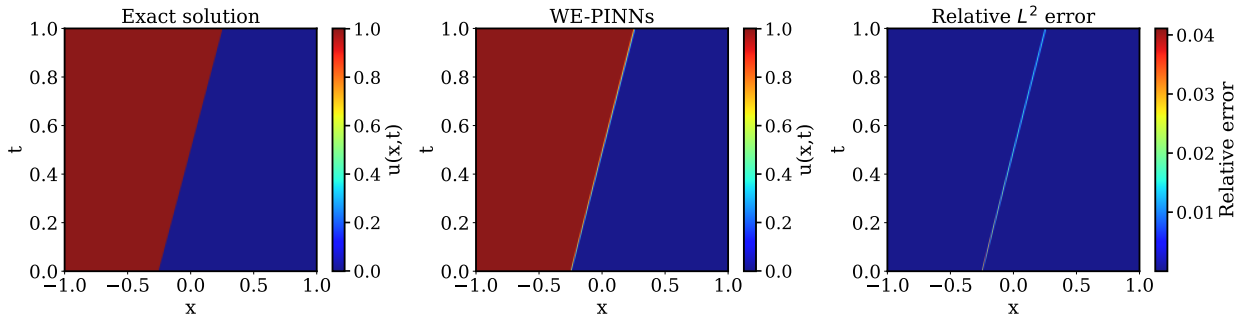


Figure 3: space–time evolution of the numerical solution for the Riemann shock problem.

Table 1: Relative errors at different times for Burgers Riemann shock problem.

| Method   | $t = 0.0$ |           |                | $t = 0.5$ |           |                | $t = 1.0$ |           |                |
|----------|-----------|-----------|----------------|-----------|-----------|----------------|-----------|-----------|----------------|
|          | $E_{L^1}$ | $E_{L^2}$ | $E_{L^\infty}$ | $E_{L^1}$ | $E_{L^2}$ | $E_{L^\infty}$ | $E_{L^1}$ | $E_{L^2}$ | $E_{L^\infty}$ |
| WE-PINNs | 8.07e-03  | 5.79e-02  | 7.95e-01       | 4.98e-03  | 3.35e-02  | 5.00e-01       | 4.32e-03  | 3.16e-02  | 4.649e-01      |
| PINNs    | 2.424e-01 | 2.438e-01 | 5.166e-01      | 1.215e-01 | 1.957e-01 | 6.680e-01      | 4.313e-02 | 1.895e-01 | 9.956e-01      |

### 5.1.2. Rarefaction

Next, we consider a rarefaction wave test with the initial condition

$$u(x, 0) = \begin{cases} 0, & x \leq -0.25, \\ 1, & x > -0.25, \end{cases}$$

Figure 4-5 shows the numerical solution at selected times. The discontinuity evolves into a smooth rarefaction fan that spreads over time with the correct self-similar structure. The solution remains stable and free of spurious oscillations or overshoots throughout the domain. The transition between the two constant states is captured accurately, and the constant regions are well preserved. The corresponding relative errors are summarized in Table 2.

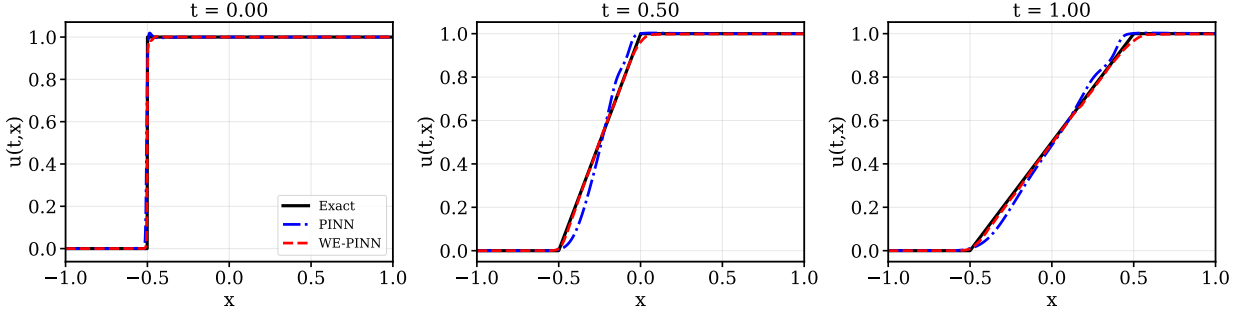


Figure 4: WE-PINNs solution of the rarefaction problem for the inviscid Burgers equation.

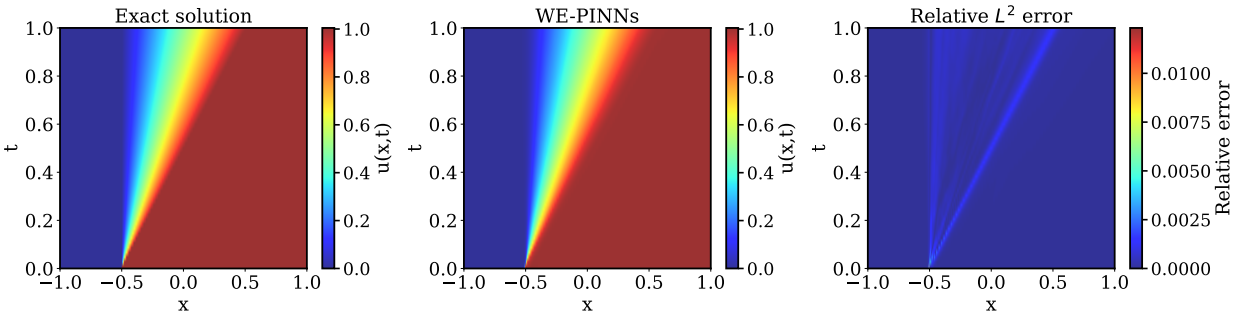


Figure 5: space-time evolution of the numerical solution for the rarefaction problem.

Table 2: Relative errors at different times for Burgers rarefaction problem.

| Method   | $t = 0.0$ |           |                | $t = 0.5$ |           |                | $t = 1.0$ |           |                |
|----------|-----------|-----------|----------------|-----------|-----------|----------------|-----------|-----------|----------------|
|          | $E_{L^1}$ | $E_{L^2}$ | $E_{L^\infty}$ | $E_{L^1}$ | $E_{L^2}$ | $E_{L^\infty}$ | $E_{L^1}$ | $E_{L^2}$ | $E_{L^\infty}$ |
| WE-PINNs | 1.702e-03 | 1.629e-02 | 3.375e-01      | 4.712e-03 | 8.243e-03 | 3.785e-02      | 1.158e-02 | 1.282e-02 | 3.214e-02      |
| PINNs    | 4.328e-03 | 4.198e-02 | 7.580e-01      | 2.798e-02 | 4.967e-02 | 1.221e-01      | 3.263e-02 | 3.918e-02 | 6.224e-02      |

### 5.1.3. Rarefaction-Shock Interaction

Finally, we consider a compactly supported initial condition

$$u(x, 0) = \begin{cases} 1, & -0.5 < x \leq 0, \\ 0, & \text{otherwise.} \end{cases}$$

This configuration produces a rarefaction wave at the left interface and a shock at the right interface. The solution undergoes a structural transition when the intermediate constant state vanishes, making this a demanding test of mixed continuous and discontinuous wave behavior. Figure 6-7 shows the numerical solution. The rarefaction fan is resolved smoothly, while the shock remains sharply localized. The method remains stable throughout the interaction and accurately captures the change in solution topology. The relative errors are summarized in Table 3.

### 5.2. Compressible Euler System

We next consider the one-dimensional compressible Euler equations, which model the motion of an inviscid compressible fluid and constitute a prototypical system of nonlinear hyperbolic conservation laws. In conservative form, the system reads

$$\partial_t \mathbf{U} + \partial_x \mathbf{F}(\mathbf{U}) = 0,$$

Table 3: Relative errors at different times for Burgers rarefaction-shock interaction problem.

| Method   | $t = 0.0$ |           |                | $t = 0.5$ |           |                | $t = 1.0$ |           |                |
|----------|-----------|-----------|----------------|-----------|-----------|----------------|-----------|-----------|----------------|
|          | $E_{L^1}$ | $E_{L^2}$ | $E_{L^\infty}$ | $E_{L^1}$ | $E_{L^2}$ | $E_{L^\infty}$ | $E_{L^1}$ | $E_{L^2}$ | $E_{L^\infty}$ |
| WE-PINNs | 1.824e-02 | 6.184e-02 | 4.943e-01      | 2.891e-02 | 4.885e-02 | 5.623e-01      | 3.124e-02 | 4.856e-02 | 4.423e-01      |
| PINNs    | 3.706e-01 | 3.016e-01 | 5.144e-01      | 3.210e-01 | 2.990e-01 | 5.303e-01      | 2.485e-01 | 2.813e-01 | 5.485e-01      |

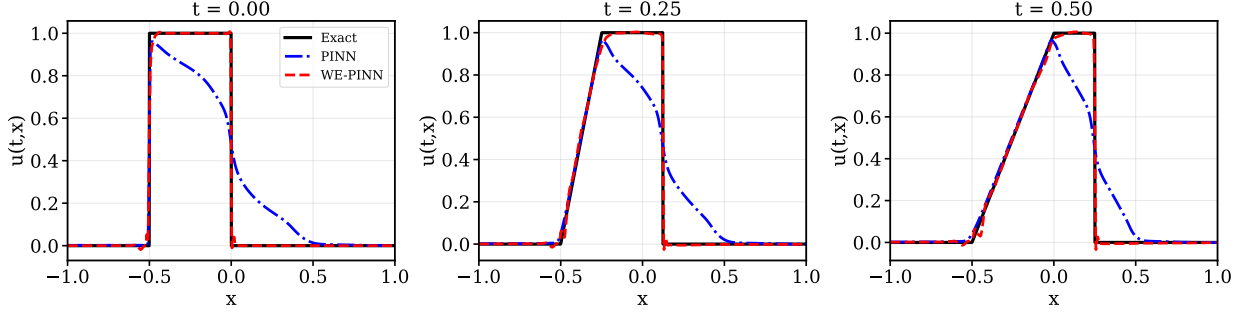


Figure 6: WE-PINNs solution of the inviscid Burgers equation for the rarefaction-shock interaction test case. The evolution shows the expansion of the rarefaction fan and the propagation of the shock.

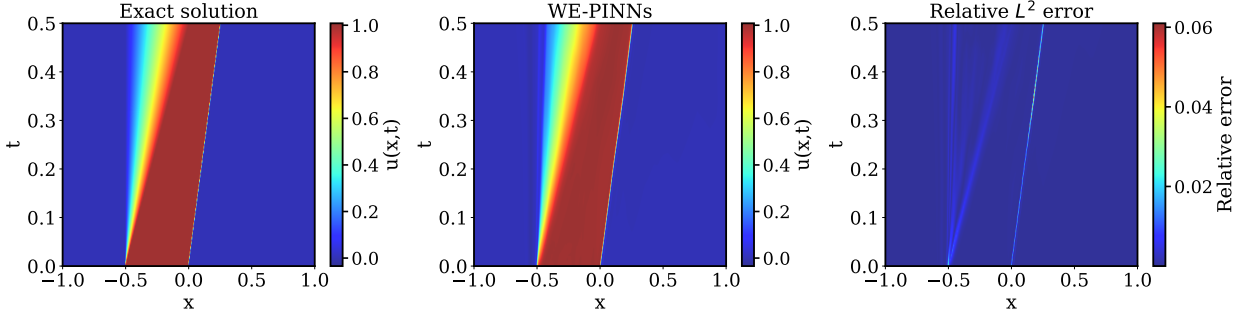


Figure 7: space–time evolution of the numerical solution for the rarefaction-shock interaction problem.

where

$$\mathbf{U} = \begin{pmatrix} \rho \\ \rho u \\ E \end{pmatrix}, \quad \mathbf{F}(\mathbf{U}) = \begin{pmatrix} \rho u \\ \rho u^2 + p \\ u(E + p) \end{pmatrix}.$$

Here,  $\rho$  denotes density,  $u$  velocity,  $p$  pressure, and  $E$  total energy. The system is closed by the ideal gas equation of state

$$E = \frac{1}{2}\rho u^2 + \frac{p}{\gamma - 1},$$

with ratio of specific heats  $\gamma > 1$ . The Euler system admits complex wave interactions, including shock waves, rarefaction waves, and contact discontinuities. Compared to scalar conservation laws, the coupled nonlinear structure and additional wave families make accurate shock resolution considerably more demanding. This system therefore provides a stringent test of the weak space–time control-volume formulation in a multi-component setting. The computational setup follows that of the previous experiments. The conserved variables are approximated directly by a neural network, and conservation is enforced through boundary flux integrals over dynamically sampled space–time control volumes. Entropy admissibility is incorporated in integral form. Training is performed using Adam pretraining followed by L-BFGS refinement. We assess the performance of WE-PINNs on a standard Riemann problem: Sod’s shock tube. This benchmark involves different combinations of shock waves, rarefactions, and contact discontinuities,

allowing evaluation of the method under varying wave strengths and interaction patterns.

### 5.2.1. Sod Shock Tube Problem

To assess the performance of WE-PINNs on systems of conservation laws, we consider the classical Sod shock tube problem for the one-dimensional compressible Euler equations. The computational domain is  $\Omega = [0, 1]$ , and the initial conditions are prescribed in terms of the primitive variables  $(\rho, u, p)$  as

$$\rho(x, 0) = \begin{cases} 1, & x \leq 0.5, \\ 0.125, & x > 0.5, \end{cases} \quad u(x, 0) = 0, \quad p(x, 0) = \begin{cases} 1, & x \leq 0.5, \\ 0.1, & x > 0.5 \end{cases}$$

with ratio of specific heats  $\gamma = 1.4$ . The entropy solution consists of a left-propagating rarefaction wave, a contact discontinuity, and a right-propagating shock wave. This benchmark evaluates the ability of the method to simultaneously resolve smooth and discontinuous wave structures in a coupled nonlinear system. In particular, accurate resolution requires capturing the shock speed and strength, preserving the sharp density jump at the contact discontinuity, and resolving the rarefaction fan without excessive diffusion (see Figures 8-9).

Table 4: Relative errors at different times for the Euler shock tube problem.

| Variable | Method   | $t = 0.01$ |           |                | $t = 0.13$ |           |                | $t = 0.2$ |           |                |
|----------|----------|------------|-----------|----------------|------------|-----------|----------------|-----------|-----------|----------------|
|          |          | $E_{L^1}$  | $E_{L^2}$ | $E_{L^\infty}$ | $E_{L^1}$  | $E_{L^2}$ | $E_{L^\infty}$ | $E_{L^1}$ | $E_{L^2}$ | $E_{L^\infty}$ |
| $\rho$   | WE-PINNs | 3.732e-03  | 1.645e-02 | 1.071e-01      | 7.857e-03  | 1.697e-02 | 1.001e-01      | 9.624e-03 | 2.167e-02 | 1.098e-01      |
|          | PINNs    | 6.599e-02  | 9.823e-02 | 3.445e-01      | 7.121e-02  | 9.093e-02 | 1.880e-01      | 8.054e-02 | 9.437e-02 | 1.518e-01      |
| $u$      | WE-PINNs | 2.578e-03  | 2.536e-02 | 7.256e-01      | 2.103e-02  | 4.813e-02 | 4.361e-01      | 1.510e-02 | 4.155e-02 | 4.476e-01      |
|          | PINNs    | 2.139e+00  | 9.600e-01 | 9.187e-01      | 3.698e-01  | 3.207e-01 | 5.649e-01      | 2.199e-01 | 2.342e-01 | 5.507e-01      |
| $p$      | WE-PINNs | 4.434e-03  | 2.049e-02 | 1.453e-01      | 6.424e-03  | 1.388e-02 | 1.377e-01      | 6.598e-03 | 1.352e-02 | 1.351e-01      |
|          | PINNs    | 6.276e-02  | 1.139e-01 | 4.357e-01      | 7.005e-02  | 8.322e-02 | 1.479e-01      | 7.700e-02 | 8.345e-02 | 1.253e-01      |
| $E$      | WE-PINNs | 4.238e-03  | 1.905e-02 | 1.421e-01      | 6.244e-03  | 1.553e-02 | 1.743e-01      | 6.385e-03 | 1.556e-02 | 1.711e-01      |
|          | PINNs    | 6.047e-02  | 1.120e-01 | 4.353e-01      | 6.836e-02  | 8.272e-02 | 1.661e-01      | 7.399e-02 | 8.328e-02 | 1.632e-01      |

### 5.3. Shallow Water Equations

The shallow water equations constitute a fundamental system of hyperbolic conservation laws used to describe the evolution of a free-surface incompressible fluid under the assumption that the horizontal length scale is significantly larger than the vertical depth. These equations arise from depth-averaging the incompressible Euler equations and are widely employed in hydrology, coastal engineering, and geophysical fluid dynamics to model phenomena such as dam-break flows, tidal motion, and tsunami propagation. In one spatial dimension, the homogeneous shallow water system can be written in conservative form as

$$\frac{\partial \mathbf{U}}{\partial t} + \frac{\partial \mathbf{F}(\mathbf{U})}{\partial x} = 0,$$

where the vector of conserved variables and the associated flux function are given by

$$\mathbf{U} = \begin{pmatrix} h \\ hu \end{pmatrix}, \quad \mathbf{F}(\mathbf{U}) = \begin{pmatrix} hu \\ hu^2 + \frac{1}{2}gh^2 \end{pmatrix}.$$

Here,  $h(x, t)$  denotes the water depth,  $u(x, t)$  the depth-averaged horizontal velocity, and  $g$  the gravitational acceleration constant. The system is strictly hyperbolic for  $h > 0$ , with eigenvalues

$$\lambda_{1,2} = u \pm \sqrt{gh},$$

which represent the propagation speeds of nonlinear gravity waves. Similar to the Euler equations, solutions of Riemann problems for the shallow water system may involve combinations of shock waves and rarefaction waves. The presence of discontinuities, as well as the requirement to preserve the positivity of the water depth, makes this

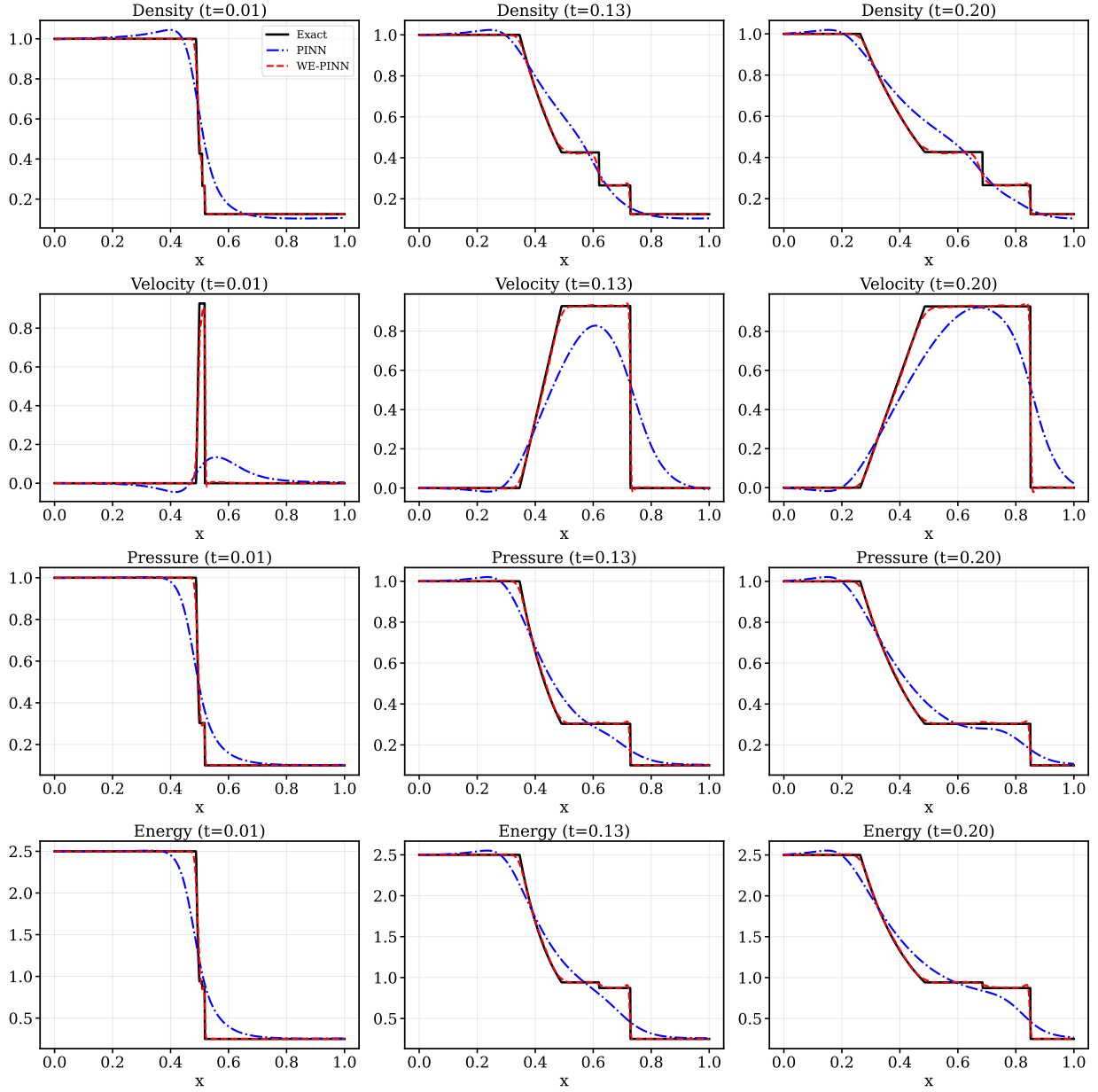


Figure 8: WE-PINNs solution of the one-dimensional Euler system for the Sod shock tube problem at  $t = 0.01, 0.13, 0.2$ . Density, velocity, energy, and pressure profiles are shown over the domain  $[-1, 1]$ .

system a demanding benchmark for numerical methods. In the following numerical experiments, we examine the ability of the proposed WE-PINNs framework to resolve complex wave interactions in shallow water flows. Particular attention is devoted to the accurate capture of hydraulic jumps (shock waves) and smooth rarefaction structures, while maintaining stability and physical admissibility of the solution.

### 5.3.1. Dam-Break Problem

To further assess the performance of the proposed method for nonlinear hyperbolic systems, we consider the classical dam-break problem for the one-dimensional shallow water equations. This test case represents a Riemann problem characterized by an initial discontinuity in the water depth, leading to the formation of nonlinear gravity

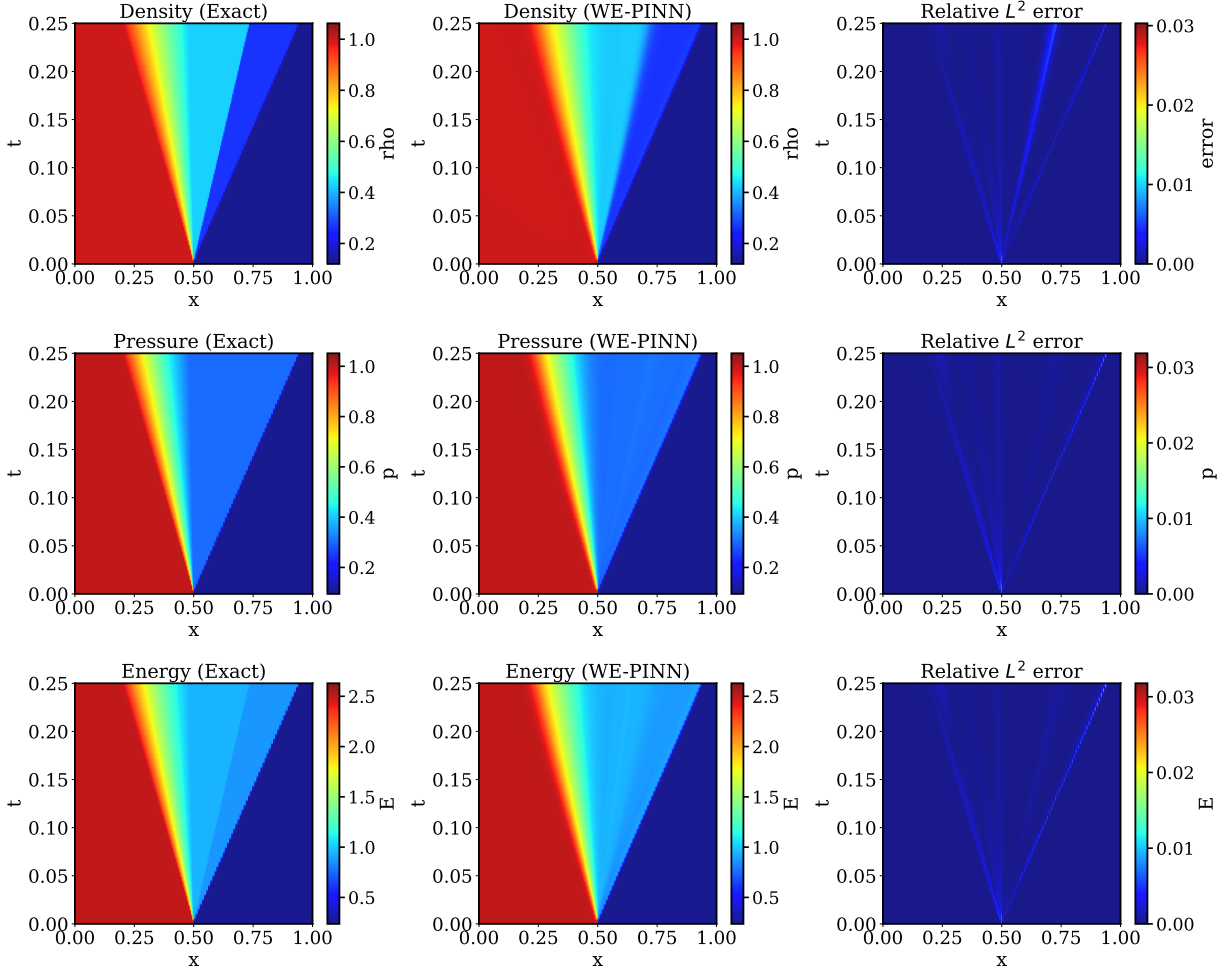


Figure 9: space–time evolution of density, pressure, and energy for the Sod shock tube problem.

waves. The computational domain is defined as  $x \in [0, 1]$ , and the initial condition is prescribed as

$$h(x, 0) = \begin{cases} 5, & x \leq 0.5 \\ 1, & x > 0.5 \end{cases}, \quad u(x, 0) = 0.$$

where  $h$  denotes the water depth and  $u$  the depth-averaged velocity. The gravitational constant  $g$  is taken as  $g = 9.81$  unless otherwise specified. This configuration corresponds to the instantaneous removal of a barrier separating two water columns of different heights. The resulting solution consists of a left-propagating rarefaction wave and a right-propagating shock wave connected through an intermediate constant state. The wave structure is self-similar and depends on the similarity variable  $\xi = x/t$ . The dam-break problem provides a stringent test for numerical methods, as it requires accurate resolution of both smooth rarefaction waves and sharp hydraulic jumps while preserving the positivity of the water depth. Figures 10-11 and Table 5 display the Quantitative comparisons with the exact Riemann solution, which are performed to evaluate the resolution properties and stability characteristics of the proposed WE-PINNs method.

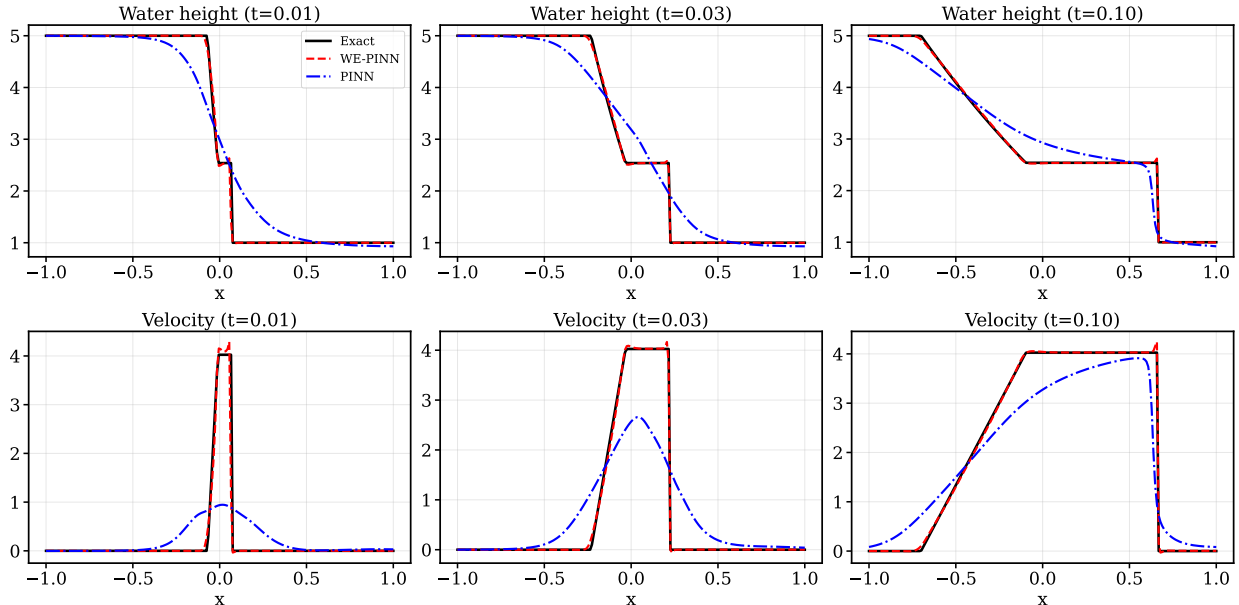


Figure 10: Numerical solution of the one-dimensional shallow water equations for the dam-break problem on the domain  $[0, 1]$ . The initial discontinuity between the left state  $h_1 = 5$  and the right state  $h_2 = 1$  generates a left-propagating rarefaction wave and a right-moving hydraulic jump. The computed depth and velocity profiles accurately reproduce the characteristic self-similar wave structure of the exact Riemann solution. The results demonstrate that the proposed WE-PINNs method effectively captures both smooth and discontinuous features while maintaining stability and preserving the positivity of the water depth.

Table 5: Relative errors at different times for the shallow water (Stoker) problem.

| Variable | Method   | $t = 0.0$ |           |                | $t = 0.05$ |           |                | $t = 0.12$ |           |                |
|----------|----------|-----------|-----------|----------------|------------|-----------|----------------|------------|-----------|----------------|
|          |          | $E_{L^1}$ | $E_{L^2}$ | $E_{L^\infty}$ | $E_{L^1}$  | $E_{L^2}$ | $E_{L^\infty}$ | $E_{L^1}$  | $E_{L^2}$ | $E_{L^\infty}$ |
| $h$      | WE-PINNs | 1.776e-03 | 6.041e-03 | 2.826e-02      | 3.481e-03  | 8.159e-03 | 2.905e-02      | 3.741e-03  | 7.258e-03 | 2.920e-02      |
|          | PINNs    | 7.084e-02 | 1.083e-01 | 2.559e-01      | 6.887e-02  | 9.144e-02 | 1.868e-01      | 7.056e-02  | 9.182e-02 | 2.722e-01      |
| $u$      | WE-PINNs | 4.787e-02 | 4.501e-02 | 5.243e-02      | 3.320e-02  | 5.014e-02 | 1.340e-01      | 9.725e-03  | 1.900e-02 | 9.216e-02      |
|          | PINNs    | 1.390e+00 | 8.151e-01 | 7.724e-01      | 6.987e-01  | 4.804e-01 | 5.284e-01      | 1.940e-01  | 2.165e-01 | 7.840e-01      |

## 6. Conclusion

We have presented WE-PINNs, a physics-informed neural network framework for the approximation of entropy solutions to nonlinear hyperbolic conservation laws. The method replaces the classical strong-form residual minimization with a space–time weak formulation derived from the divergence theorem, enforcing conservation through boundary flux integrals over dynamically sampled space–time control volumes. Entropy admissibility is incorporated in integral form via a one-sided penalty that selects the physically relevant weak solution without suppressing shock dissipation. The resulting loss functional is mesh-free, avoids explicit differentiation of the neural approximation, and remains well-defined in the presence of discontinuities. Furthermore, the method is remarkably easy to implement as it relies solely on a simple feedforward neural network without the need for auxiliary networks or complex saddle-point optimization. We have established a rigorous convergence analysis framework for scalar conservation laws, demonstrating that the  $L^1$  error towards the entropy solution is explicitly controlled by the dual norm formulation of our discrete losses.

Numerical experiments on three benchmark problems, the inviscid Burgers equation, the compressible Euler equations, and the shallow water equations, demonstrate that WE-PINNs accurately resolve shock waves, rarefaction fans, and contact discontinuities in both scalar and system settings. The method remains stable across smooth and shock-dominated regimes without requiring artificial viscosity or explicit shock tracking.

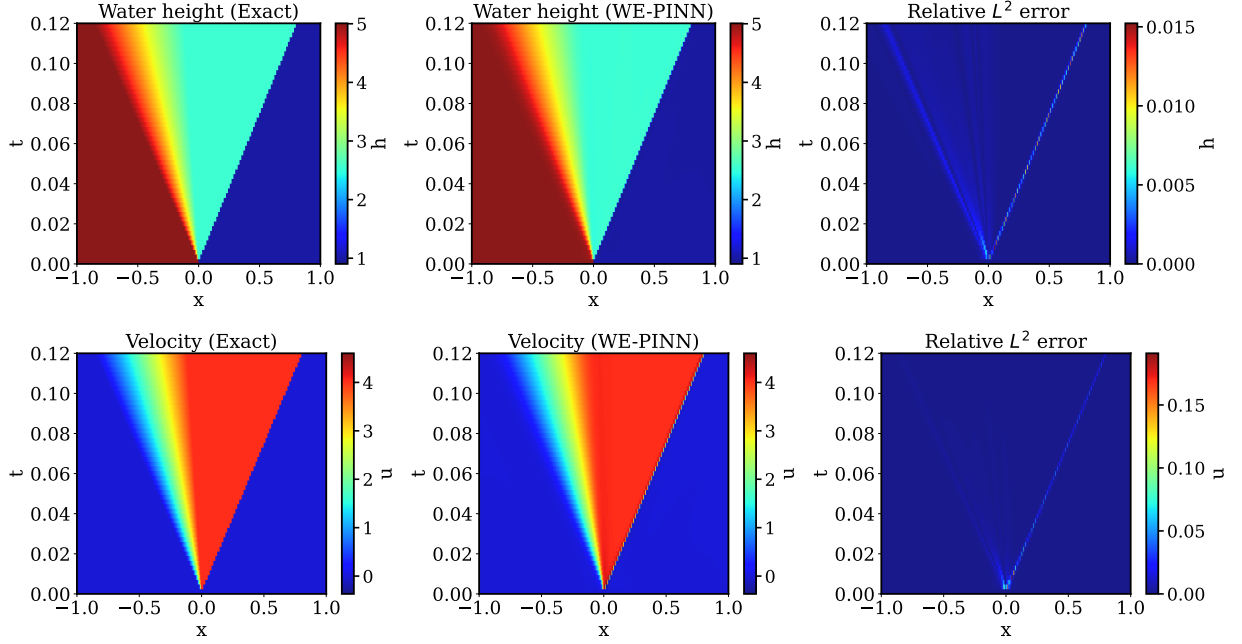


Figure 11: space–time evolution of water depth and velocity for the dam-break problem.

These results open several directions for future research, including extending the convergence analysis to systems of conservation laws, which remains an important open problem. Additionally, adaptive strategies for selecting loss weights and more efficient quadrature schemes will be investigated to further improve computational efficiency.

## Appendix A

In this section, we write the space–time conservation identity

$$\int_{\partial D} (Un_t + F(U) \cdot n_x) dS = 0$$

explicitly for axis-aligned rectangular space–time subdomains. These formulas make clear how conservation is enforced over control volumes in different spatial dimensions.

*1D space: rectangles in  $(x, t)$*

Let  $d = 1$  and consider the space–time rectangle

$$D = [x_1, x_2] \times [t_1, t_2].$$

The boundary  $\partial D$  consists of four edges: two time-like edges ( $t = t_1$  and  $t = t_2$ ) and two space-like edges ( $x = x_1$  and  $x = x_2$ ). Applying the space–time conservation identity yields

$$\begin{aligned} & \int_{x_1}^{x_2} U(x, t_2) dx - \int_{x_1}^{x_2} U(x, t_1) dx \\ & + \int_{t_1}^{t_2} F(U(x_2, t)) dt - \int_{t_1}^{t_2} F(U(x_1, t)) dt = 0. \end{aligned}$$

This expression states that the change of the conserved quantity inside the spatial interval  $[x_1, x_2]$  between times  $t_1$  and  $t_2$  is exactly balanced by the flux entering and leaving through the spatial boundaries.

2D space: boxes in  $(x, y, t)$

Let  $d = 2$  and consider the space–time box

$$D = [x_1, x_2] \times [y_1, y_2] \times [t_1, t_2].$$

The boundary  $\partial D$  now consists of six faces: two time faces and four spatial faces. The conservation identity becomes

$$\begin{aligned} & \int_{x_1}^{x_2} \int_{y_1}^{y_2} U(x, y, t_2) dx dy - \int_{x_1}^{x_2} \int_{y_1}^{y_2} U(x, y, t_1) dx dy \\ & + \int_{t_1}^{t_2} \int_{y_1}^{y_2} F^{(1)}(U(x_2, y, t)) dy dt - \int_{t_1}^{t_2} \int_{y_1}^{y_2} F^{(1)}(U(x_1, y, t)) dy dt \\ & + \int_{t_1}^{t_2} \int_{x_1}^{x_2} F^{(2)}(U(x, y_2, t)) dx dt - \int_{t_1}^{t_2} \int_{x_1}^{x_2} F^{(2)}(U(x, y_1, t)) dx dt = 0. \end{aligned}$$

As in the one-dimensional case, the variation of the conserved quantities inside the spatial region  $[x_1, x_2] \times [y_1, y_2]$  over the time interval  $[t_1, t_2]$  is balanced by the fluxes across all spatial faces.

3D space: boxes in  $(x, y, z, t)$

Let  $d = 3$  and consider the space–time box

$$D = [x_1, x_2] \times [y_1, y_2] \times [z_1, z_2] \times [t_1, t_2].$$

The boundary  $\partial D$  consists of eight faces: two time faces and six spatial faces. The conservation identity reads

$$\begin{aligned} & \int_{x_1}^{x_2} \int_{y_1}^{y_2} \int_{z_1}^{z_2} U(x, y, z, t_2) dx dy dz - \int_{x_1}^{x_2} \int_{y_1}^{y_2} \int_{z_1}^{z_2} U(x, y, z, t_1) dx dy dz \\ & + \int_{t_1}^{t_2} \int_{y_1}^{y_2} \int_{z_1}^{z_2} F^{(1)}(U(x_2, y, z, t)) dy dz dt - \int_{t_1}^{t_2} \int_{y_1}^{y_2} \int_{z_1}^{z_2} F^{(1)}(U(x_1, y, z, t)) dy dz dt \\ & + \int_{t_1}^{t_2} \int_{x_1}^{x_2} \int_{z_1}^{z_2} F^{(2)}(U(x, y_2, z, t)) dx dz dt - \int_{t_1}^{t_2} \int_{x_1}^{x_2} \int_{z_1}^{z_2} F^{(2)}(U(x, y_1, z, t)) dx dz dt \\ & + \int_{t_1}^{t_2} \int_{x_1}^{x_2} \int_{y_1}^{y_2} F^{(3)}(U(x, y, z_2, t)) dx dy dt - \int_{t_1}^{t_2} \int_{x_1}^{x_2} \int_{y_1}^{y_2} F^{(3)}(U(x, y, z_1, t)) dx dy dt = 0. \end{aligned}$$

This formula expresses conservation over a three-dimensional spatial control volume evolving in time. The total variation of the conserved variables inside the volume is exactly balanced by the fluxes through the six spatial faces.

## Appendix B

### Two-Dimensional Shallow-Water Equations

The two-dimensional shallow water equations (SWE) are considered in conservative vector form:

$$\frac{\partial \mathbf{U}}{\partial t} + \frac{\partial \mathbf{F}(\mathbf{U})}{\partial x} + \frac{\partial \mathbf{G}(\mathbf{U})}{\partial y} = 0, \quad (4)$$

where

$$\mathbf{U} = \begin{pmatrix} h \\ hu \\ hv \end{pmatrix}, \quad \mathbf{F}(\mathbf{U}) = \begin{pmatrix} hu \\ hu^2 + \frac{1}{2}gh^2 \\ huv \end{pmatrix}, \quad \mathbf{G}(\mathbf{U}) = \begin{pmatrix} hv \\ huv \\ hv^2 + \frac{1}{2}gh^2 \end{pmatrix}. \quad (5)$$

Here,  $h(x, y, t)$  denotes the water depth,  $(u, v)$  are the velocity components, and  $g = 9.81$  is the gravitational acceleration. The computational domain is  $(x, y) \in [-1, 1]^2$ . The initial velocity is zero,  $u(x, y, 0) = 0$  and  $v(x, y, 0) = 0$ . Two

discontinuous dam-break configurations are considered. For the diagonal dam-break case, the interface is defined by  $\phi(x, y) = x + y$ , and the initial condition for the water height is

$$h(x, y, 0) = \begin{cases} h_L, & \phi(x, y) < 0, \\ h_R, & \phi(x, y) \geq 0, \end{cases} \quad (6)$$

with  $h_L = 5$  and  $h_R = 1$ . For the circular dam-break case, the interface is defined by

$$\phi(x, y) = \sqrt{(x - x_c)^2 + (y - y_c)^2} - R, \quad (7)$$

with  $(x_c, y_c) = (0, 0)$  and  $R = 0.5$ , and the same piecewise definition is used for  $h(x, y, 0)$ . Results are reported in Figs. 12 and 13.

### Two-Dimensional Euler Equations

The two-dimensional compressible Euler equations are considered in conservative vector form:

$$\frac{\partial \mathbf{U}}{\partial t} + \frac{\partial \mathbf{F}(\mathbf{U})}{\partial x} + \frac{\partial \mathbf{G}(\mathbf{U})}{\partial y} = 0, \quad (8)$$

where

$$\mathbf{U} = \begin{pmatrix} \rho \\ \rho u \\ \rho v \\ E \end{pmatrix}, \quad \mathbf{F}(\mathbf{U}) = \begin{pmatrix} \rho u \\ \rho u^2 + p \\ \rho uv \\ u(E + p) \end{pmatrix}, \quad \mathbf{G}(\mathbf{U}) = \begin{pmatrix} \rho v \\ \rho uv \\ \rho v^2 + p \\ v(E + p) \end{pmatrix}. \quad (9)$$

Here,  $\rho(x, y, t)$  denotes the density,  $(u, v)$  the velocity components,  $p$  the pressure, and  $E$  the total energy given by

$$E = \frac{p}{\gamma - 1} + \frac{1}{2}\rho(u^2 + v^2), \quad (10)$$

with  $\gamma = 1.4$ . The computational domain is  $(x, y) \in [-1, 1]^2$ . Two discontinuous initial configurations are considered. For the first test (2D Riemann problem), the domain is divided into four quadrants, with piecewise constant states defined as

$$(\rho, u, v, p)(x, y, 0) = \begin{cases} (2.0, 0.75, 0.5, 1.0), & x \leq 0, y > 0, \\ (1.0, 0.75, -0.5, 1.0), & x > 0, y > 0, \\ (1.0, -0.75, 0.5, 1.0), & x \leq 0, y \leq 0, \\ (3.0, -0.75, -0.5, 1.0), & x > 0, y \leq 0. \end{cases} \quad (11)$$

For the second test, the Radially symmetric Riemann problem, the interface is defined by

$$\phi(x, y) = \sqrt{x^2 + y^2} - R, \quad (12)$$

with  $R = 0.13$ . The initial condition is given by

$$(\rho, u, v, p)(x, y, 0) = \begin{cases} (2.0, 0, 0, 15.0), & \phi(x, y) < 0, \\ (1.0, 0, 0, 1.0), & \phi(x, y) \geq 0. \end{cases} \quad (13)$$

Results are reported in Figs. 14 and 15.

## Appendix C

The convex entropy pairs  $(\eta, q)$  associated with the considered systems are defined as follows.

**Burgers equation:**

$$\eta(u) = \frac{u^2}{2}, \quad q(u) = \frac{u^3}{3},$$

where  $u$  denotes the scalar state variable.

**Compressible Euler equations:**

$$\eta(U) = -\rho s, \quad q(U) = -\rho \mathbf{u} s,$$

where  $\rho$  is the density,  $\mathbf{u}$  is the velocity vector, and  $s$  is the specific entropy defined, for an ideal gas, by

$$s = \ln\left(\frac{p}{\rho^\gamma}\right),$$

with  $p$  the pressure and  $\gamma$  the ratio of specific heats.

**Shallow water equations:**

$$\eta(U) = \frac{1}{2}h|\mathbf{u}|^2 + \frac{1}{2}gh^2, \quad q(U) = \eta(U) \mathbf{u},$$

where  $h$  denotes the water height,  $\mathbf{u}$  is the velocity vector, and  $g$  is the gravitational constant.

In all cases, the entropy functions are convex and the corresponding entropy fluxes satisfy the compatibility condition with the physical flux, ensuring consistency with the entropy inequality.

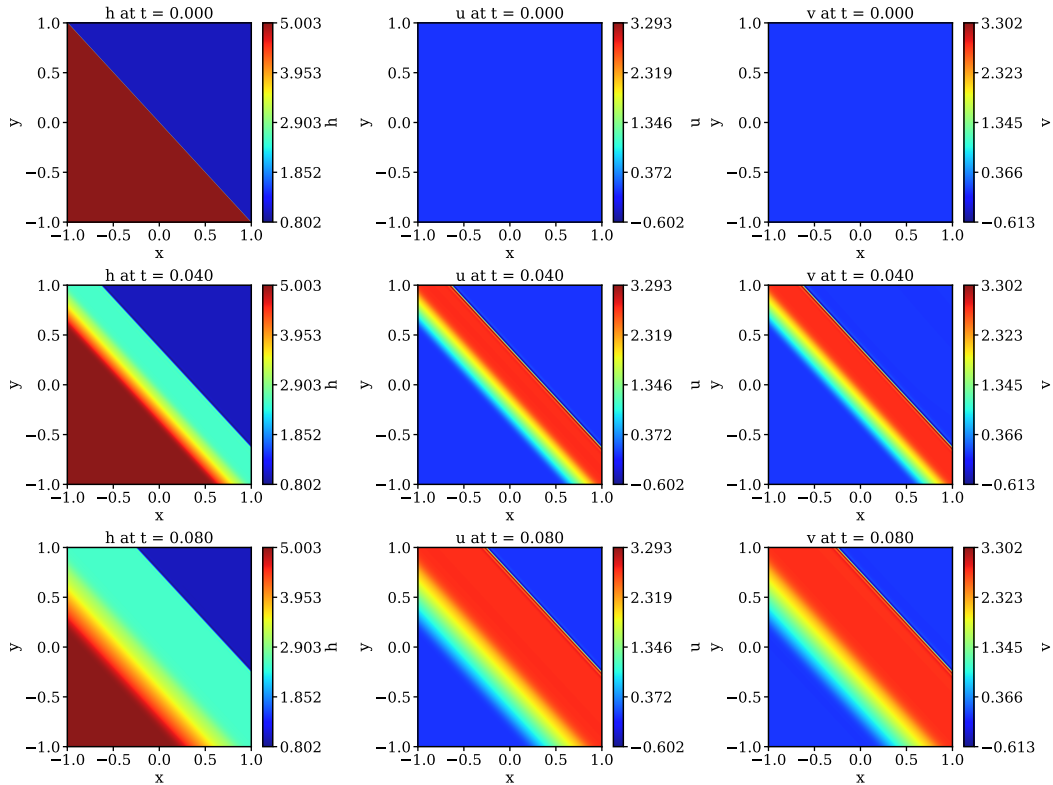


Figure 12: WE-PINNs solution of the two-dimensional SWE for the diagonal dam-break problem at  $t = 0.00, 0.04,$  and  $0.08$ . Shown are the water depth  $h$  and velocity components  $u$  and  $v$ .

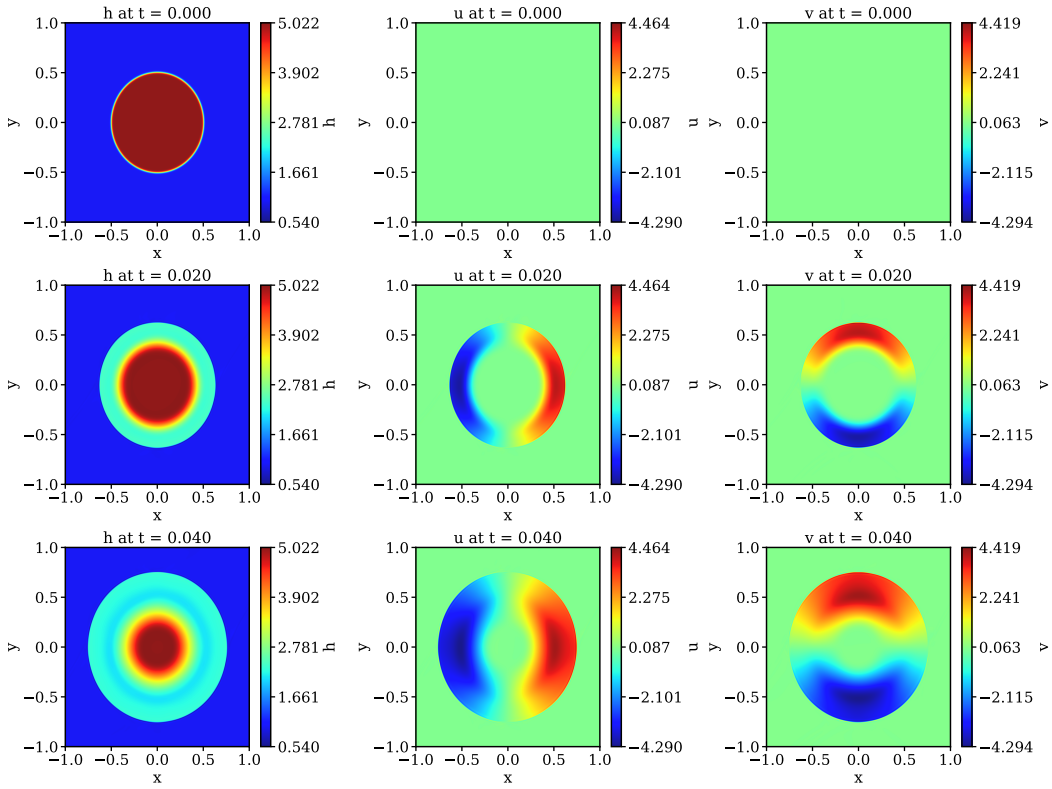


Figure 13: WE-PINNs solution of the two-dimensional SWE for the circular dam-break problem at  $t = 0.00, 0.02,$  and  $0.04$ . Shown are the water depth  $h$  and velocity components  $u$  and  $v$ .

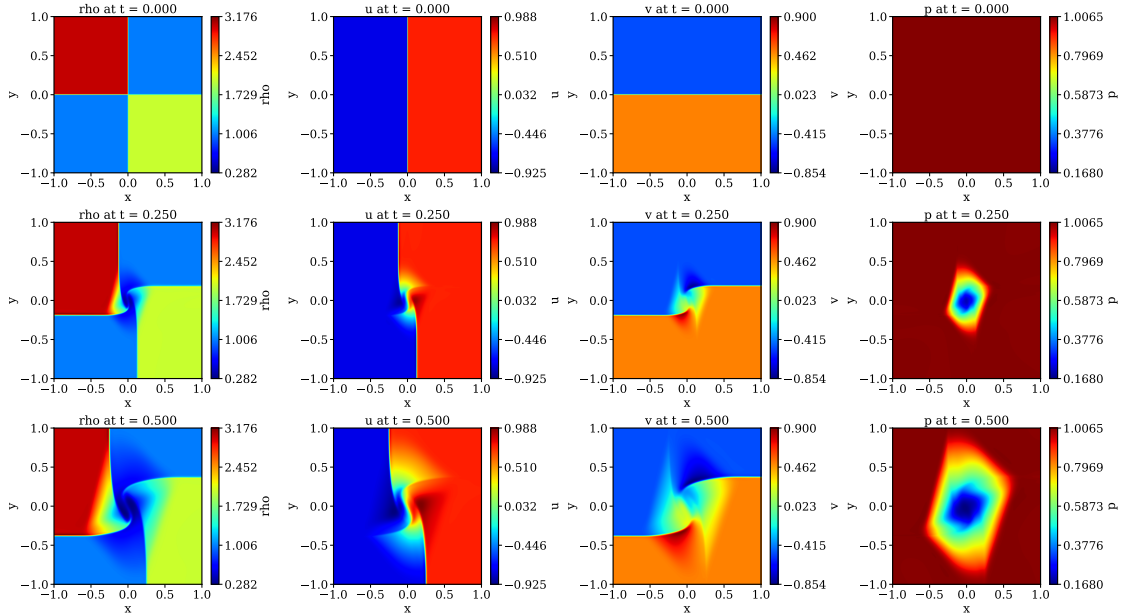


Figure 14: WE-PINNs solution of the two-dimensional Euler equations for the quadrant Riemann problem. Shown are the density  $\rho$ , velocity components  $u, v$ , and pressure  $p$ .

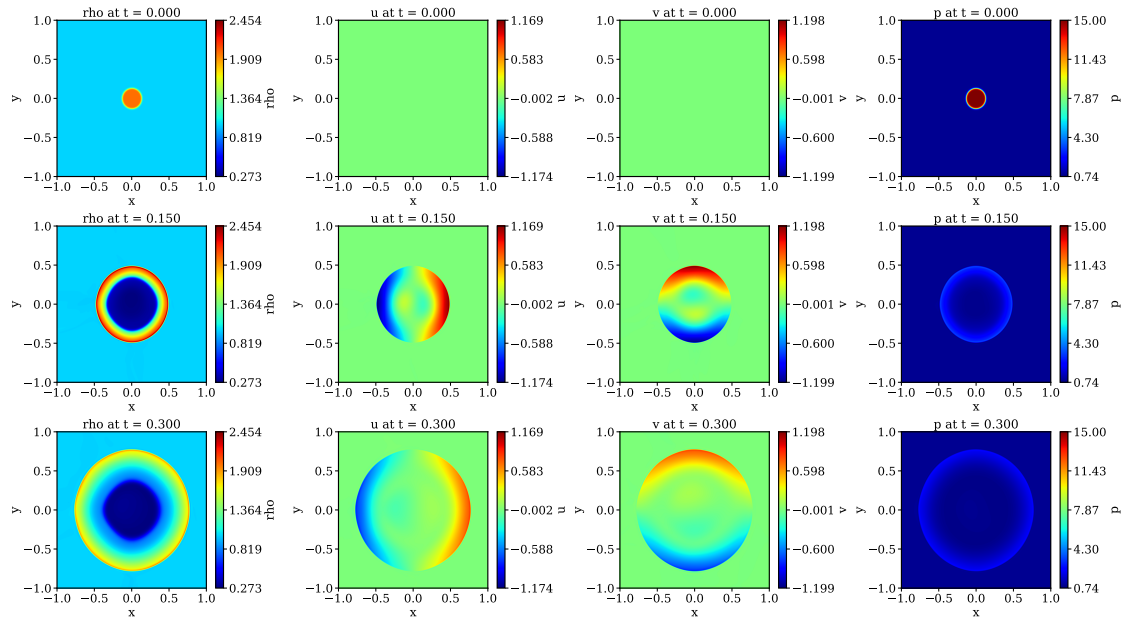


Figure 15: WE-PINNs solution of the two-dimensional Euler equations for The Radially symmetric Riemann problem. Shown are the density  $\rho$ , velocity components  $u$ ,  $v$ , and pressure  $p$ .

## References

- [1] P. D. Lax, *Hyperbolic Systems of Conservation Laws and the Mathematical Theory of Shock Waves*, SIAM, 1973.
- [2] R. J. LeVeque, *Finite Volume Methods for Hyperbolic Problems*, Cambridge University Press, 2002.
- [3] C. M. Dafermos, *Hyperbolic Conservation Laws in Continuum Physics*, Springer, 2016.
- [4] E. F. Toro, *Riemann Solvers and Numerical Methods for Fluid Dynamics: A Practical Introduction*, 3rd Edition, Springer, 2009.
- [5] W. Aboussi, M. Ziggaf, I. Kissami, M. Boubekeur, A highly efficient finite volume method with a diffusion control parameter for hyperbolic problems, *Mathematics and Computers in Simulation* 213 (2023) 177–193.
- [6] P. D. Lax, Hyperbolic systems of conservation laws ii, *Communications on Pure and Applied Mathematics* 10 (1957) 537–566.
- [7] J. Glimm, Solutions in the large for nonlinear hyperbolic systems of equations, *Communications on Pure and Applied Mathematics* 18 (1965) 697–715.
- [8] A. Bressan, *Hyperbolic systems of conservation laws: the one-dimensional Cauchy problem*, Vol. 20, OUP Oxford, 2000.
- [9] S. N. Kružkov, First order quasilinear equations with several independent variables, *Mathematics of the USSR-Sbornik* 10 (1970) 217–243.
- [10] M. Raissi, P. Perdikaris, G. E. Karniadakis, Physics-informed neural networks: A deep learning framework for solving forward and inverse problems involving nonlinear partial differential equations, *Journal of Computational Physics* 378 (2019) 686–707.
- [11] S. Cai, Z. Mao, Z. Wang, M. Yin, G. E. Karniadakis, Physics-informed neural networks (pinns) for fluid mechanics: A review, *Acta Mechanica Sinica* 37 (12) (2021) 1727–1738.

- [12] G. E. Karniadakis, I. G. Kevrekidis, L. Lu, P. Perdikaris, S. Wang, L. Yang, Physics-informed machine learning, *Nature Reviews Physics* 3 (6) (2021) 422–440.
- [13] S. Cuomo, V. S. Di Cola, F. Giampaolo, G. Rozza, M. Raissi, F. Piccialli, Scientific machine learning through physics–informed neural networks: Where we are and what’s next, *Journal of Scientific Computing* 92 (3) (2022) 88.
- [14] Z. Mao, A. D. Jagtap, G. E. Karniadakis, Physics-informed neural networks for high-speed flows, *Computer Methods in Applied Mechanics and Engineering* 360 (2020) 112789.
- [15] A. D. Jagtap, E. Kharazmi, G. E. Karniadakis, Conservative physics-informed neural networks on discrete domains for conservation laws, *Computer Methods in Applied Mechanics and Engineering* 365 (2020) 113028.
- [16] O. Fuks, H. A. Tchelepi, Limitations of physics informed machine learning for nonlinear two-phase transport in porous media, *Journal of Machine Learning for Modeling and Computing* 1 (1) (2020).
- [17] T. De Ryck, S. Mishra, R. Molinaro, wpinns: Weak physics informed neural networks for approximating entropy solutions of hyperbolic conservation laws, *SIAM Journal on Numerical Analysis* 62 (2) (2024) 811–841.
- [18] Y. Wang, S. Yang, Coupled integral pinn for conservation law, *arXiv preprint arXiv:2411.11276* (2024).
- [19] S. Wang, Y. Teng, P. Perdikaris, Understanding and mitigating gradient flow pathologies in physics-informed neural networks, *SIAM Journal on Scientific Computing* 43 (5) (2021) A3055–A3081.
- [20] R. G. Patel, I. Manickam, N. A. Trask, M. A. Wood, M. Lee, I. Tomas, E. C. Cyr, Thermodynamically consistent physics-informed neural networks for hyperbolic systems, *Journal of Computational Physics* 449 (2022) 110754.
- [21] T. Zhu, B. Si, L. Fu, Y. Lu, Sfvnet: Finite-volume informed u-net for compressible flow prediction with sparse data under ill-conditions, *Journal of Computational Physics* (2026) 114696.
- [22] A. Chaumet, J. Giesselmann, Improving weak pinns for hyperbolic conservation laws: Dual norm computation, boundary conditions and systems, *SMAI Journal of Computational Mathematics* 10 (2024) 373–401. doi: 10.5802/smai-jcm.116.
- [23] X. Wang, S. Yi, H. Gu, J. Xu, W. Xu, Wf-pinns: solving forward and inverse problems of burgers equation with steep gradients using weak-form physics-informed neural networks, *Scientific Reports* 15 (1) (2025) 40555.
- [24] F. Bouchut, B. Perthame, Kruzkov’s estimates for scalar conservation laws revisited, *Transactions of the American Mathematical Society* 350 (7) (1998) 2847–2870.
- [25] D. P. Kingma, J. Ba, Adam: A method for stochastic optimization, *arXiv preprint arXiv:1412.6980* (2014).
- [26] D. C. Liu, J. Nocedal, On the limited memory bfgs method for large scale optimization, *Mathematical programming* 45 (1) (1989) 503–528.
- [27] J. Nocedal, Updating quasi-newton matrices with limited storage, *Mathematics of computation* 35 (151) (1980) 773–782.